INTERFEROMETRIC MEASUREMENT OF THE ZEEMAN EFFECT OF HELIUM INFRARED LINES

A Thesis

Submitted to the Faculty

of

Colorado School of Mines

by

Hung-Liang Lin

In Partial Fulfillment of the

Requirements for the Degree

of

Master of Science

November, 1974

A Thesis submitted to the Faculty and the Board of Trustees of the Colorado School of Mines in partial fulfillment of the requirements for the degree of Master of Science (Physics).

Signed: _____
Student

Golden, Colorado
Date: Dec 2, 1974

Approved: _____
Thesis Advisor

_____
Head of Department

Golden, Colorado
Date: Dec 2, 1974

ACKNOWLEDGEMENT

The author is very grateful to Dr. Kline for his guidance and assistance in the research work and writing. The author also appreciates the help generously given by the rest of the Physics faculty and by Mr. Kintner.

ABSTRACT

The principal aim of this work is to develop an electronic amplification system for high resolution spectroscopy using a variable spacing Fabry-Perot interferometer in the near infra-red region. A novel system has been designed and built which compensates for the inherently noisy signal of the PbS photo-cell. This has been used to study the Zeeman effect of the He 1μ and 2μ lines.

CONTENTS

I. INTRODUCTION

I-1. DETECTION OF INFRARED RADIATION

In 1800 Sir William Herschel discovered the heating of a thermometer placed beyond the end of the visible solar spectrum. He showed that the radiation causing this heating obeys the laws of optics, but progress was slow because of the lack of sensitive and accurate detectors. The thermocouple was first used by L. Nobile in 1830, photographic plates were sensistized to infrared in 1880 by W. Abney, and S. Langley first applied a bolometer in 1881. W. Smith discovered the photoconductive effect in 1873. The history of these developments is well summarized in McGucken[1], McQuister[2], Avery[3], and Hasmer[4].

Lead sulfide cells were first developed in Germany before World War II. Since 1940 much work has been done on various photoconductive materials such as PbS, PbSe, InAs, and doped Si, Tl and Ge. More detailed description of several infrared detectors will be given in the following sections.

I-1.1 THERMAL DETECTORS

Infrared detectors[2,5] can be divided into two fundamental types, thermal detectors and photon detectors. In a thermal detector, the radiation is absorbed, changing the temperature of the

device, which then permits detection by change of some other property. The advantage of thermal detectors is the uniform response over a wide wavelength range.

Thermocouple Detectors: The contact potential at the junction of two dissimilar metals is a weak function of temperature. When two such junctions are joined into a circuit, the small difference in potential can be detected when the junctions are maintained at different temperatures. When radiation is received by a blackened junction, the resulting emf can be calibrated to give the intensity of the radiation. A thermopile has several pairs of junctions in series and hence gives greater responsivity.[6] The signal available for a weak light source is very small, and it is difficult to provide electronic amplification at the very low frequencies required by the slow response time of this detector.

Pneumatic Detectors:[7] Golay detectors have a volume of gas confined against a flexible membrane. When radiation is received, the increased temperature of the gas causes a slight distension of the membrane. This may be detected by a capacitive transducer, or by the change in the amount of light reflected from the membrane onto a photocell. This detector is more sensitive in the normal infrared region than thermocouples, but much less sensitive in the near infrared than photoconductive cells.

Bolometer Detectors:[4] A bolometer measures the radiant power by measuring the change of resistance due to temperature changes. For sensitivity it is made of semiconductor materials, or is kept barely superconducting. The response time is about the same as that of a thermocouple.

I-1.2 PHOTON DETECTORS

The most significant advantage of photodetectors is their slight dependence on temperature effects, which reduces the importance of the conditions of thermal equalibrium under which they are used. Usually the time constant is smaller, so that higher frequency amplification can be used. There is a fundamental limitation due to the fact that minimum photon energy must be available for the photoelectric process. Photon detectors have been built which rely on photographic, photoemissive, photoconductive, and photoelectromagnetic effects.

Photography[8,2]: The original photographic emulsions were sensitive only to blue and ultraviolet light. In 1873 H. W. Vogel discovered that addition of dyes to the emulsion could extend response toward the red, but at present sensitivity remains very low at 1μ and no method is known to extend sensitivity beyond 1.4μ.

Photoemissive Detectors: Emission of photoelectrons was discovered by H. Hertz[10] in 1887 in his monumental work verifying Maxwell's equations. The results were explained by Einstein[11] in 1905, and fully verified by Millikan[12]. The energy of an emitted electron is a linear function of the frequency as shown in Equation(1) and is independent of the intensity of the light. No emission will occur if the photon energy is less than the work function $e\phi$. The photocurrent is proportional to the intensity of the light received.

$$W = h\nu - e\phi \qquad (1)$$

In order to detect infrared radiation, a material of low work

function is needed. There are a few materials which can respond beyond the red end of the spectrum, in particular Ag-O-Cs has a work function below 1 eV and can respond to about 1.2 μ.

Photoconductive Detectors: In the photoconductive effect, photons transfer enough energy to electrons in a crystal to free them from a bound state so that they can contribute to the conductivity of the material. The military usefulness of these materials has contributed to their rapid development. The most important photoconductive materials are PbS[13], which responds up to 3μ, PbTe (5.2μ), InSb (7.5μ), and Ge[14] doped with Au (7 μ). Characteristic curves are given for several materials in Figure 1. Since PbS shows the highest sensitivity in the region of current interest, further discussion will be limited to these cells.

I-1.3 LEAD SULFIDE PHOTO-CELLS

Lead sulfide photocells[13] are usually made as amorphous films[15] rather than single crystals[16] because of ease of production. These films are either deposited chemically or by evaporation in vacuum. We have made some chemically deposited cells which worked satisfactorily. In either method of production, the oxygen content of the film is critical, and the crystal size is also important. The mechanism of photoconductivity in PbS has been explained in detail by Slater[17] and others[18,19,20,21]. The theory of noise in PbS cells has been studied by Petritz[20] and by Spencer[21,23]. While PbS has excellent performance at room temperatures, the signal to noise ratio increases significantly with decreasing temperature. This is shown in Figure 2.

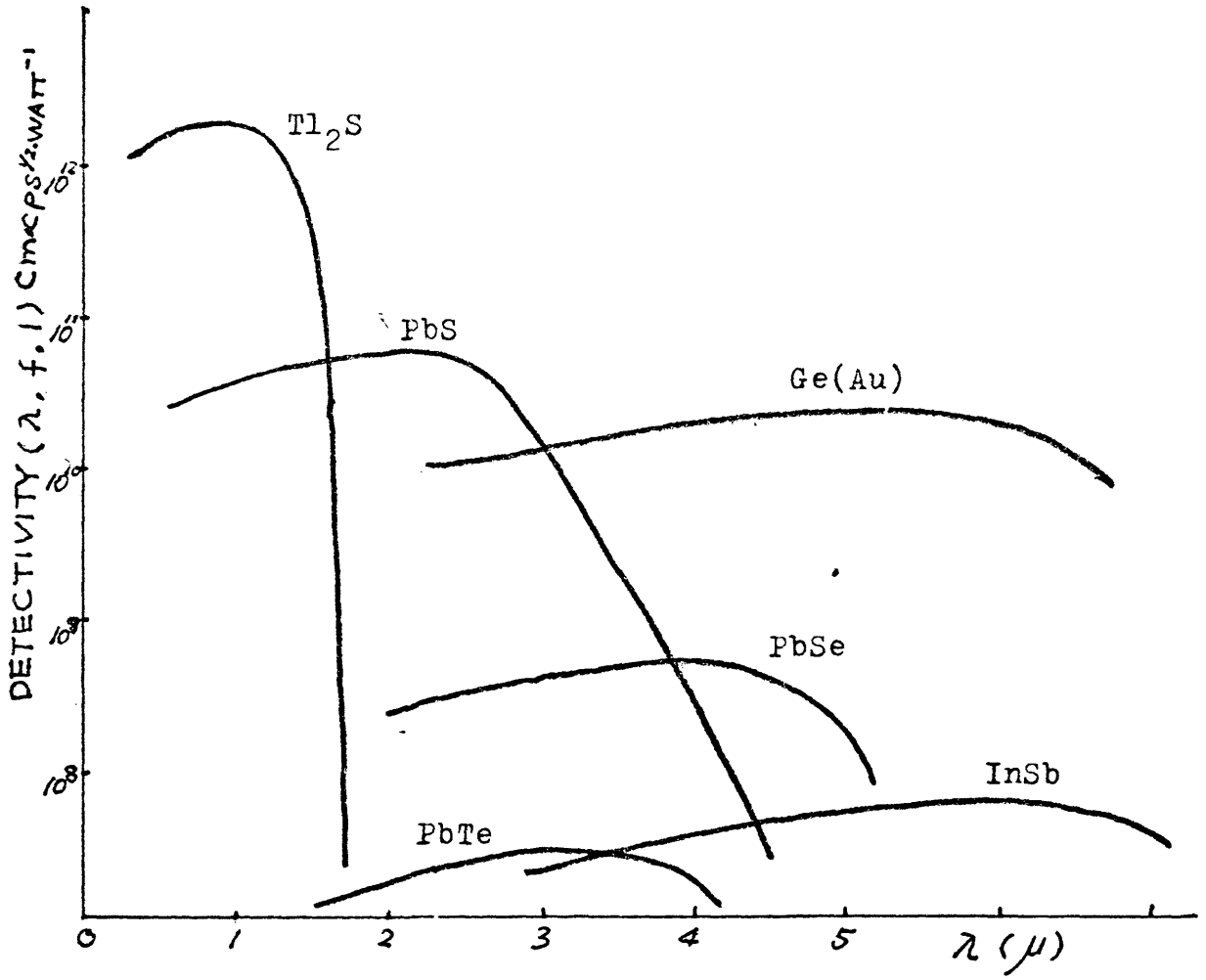

Fig.1 SPECTRAL DETECTIVITY OF SOME PHOTO-CONDUCTORS AT ROOM TEMPERATURE

Under constant illumination, both signal and noise are directly proportional to the voltage difference across the cell until the point where the current heats the cell, increases the thermal noise and limits the signal. Clearly, PbS cells are current noise limited, so that the applied voltage can be increased until the signal to noise ratio starts to decrease. Experimentally, under constant illumination, the signal to noise ratio is inversely proportional to the square root of the cell area. For given film thickness, the resistance does not change with increasing size (keeping the same shape), while the heat dissipation increases with area, so a larger potential can be applied to a larger cell before the signal to noise ratio will decrease. Hence it is important to make a proper choice of cell size and driving potential.

The time constant of a PbS photocell is about 200 μsec at room temperature, increasing with lower temperature. Figure 3 shows the relative signal voltage (AC) as a function of chopping frequency. Both because much of the noise in the cell grows as 1/f, and because the electronic problems are more easily solved with higher frequency, it is clear that the best chopping frequency would be somewhat above 100 Hz. In order to avoid harmonics of line frequency, 150 Hz has been used with a synchronous drive motor and five blades, or the belt driven Princeton Applied Research commercial unit is now used, with chopping frequency 104 Hz or 208 Hz.

Fig.2 Spectral detectivity of PbS at various temperature

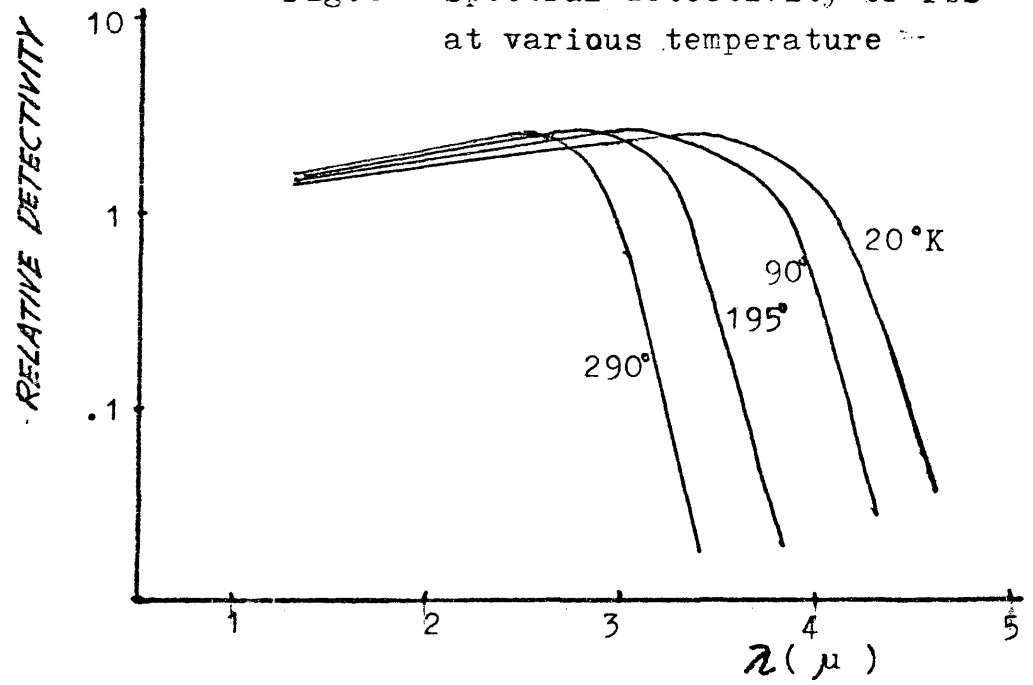

Fig.3 Frequency Response of PbS at room Temperature

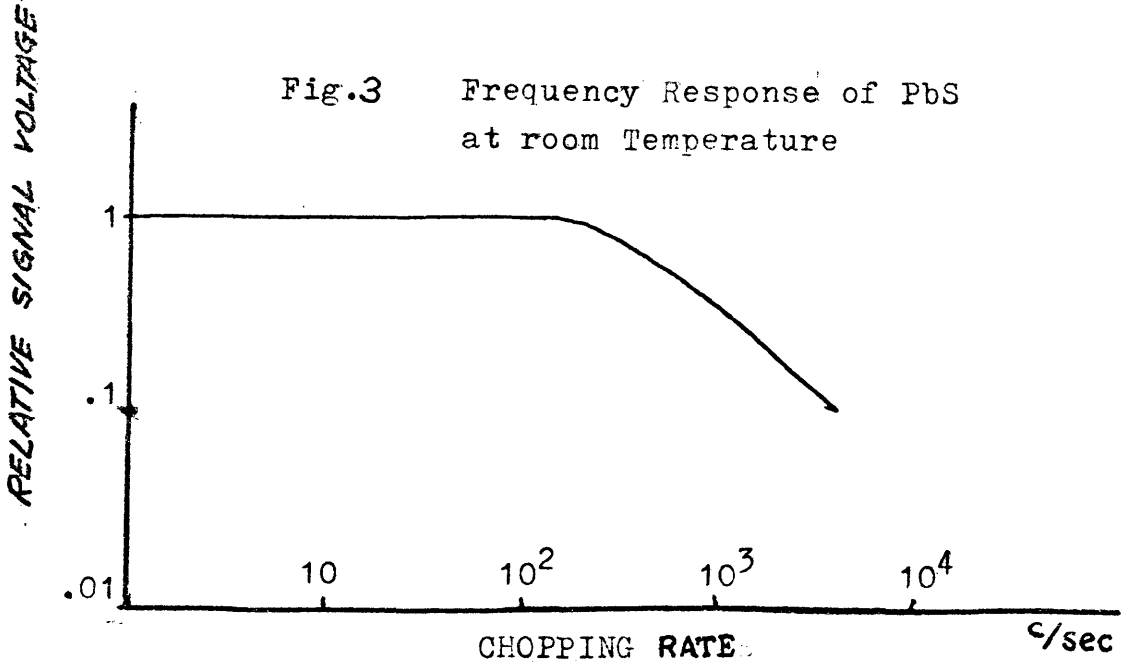

I-2. THE APPLICATION OF THE FABRY-PEROT INTERFEROMETER IN THE INFRARED

I-2.1 THEORY OF THE FABRY-PEROT INTERFEROMETER

The Fabry-Perot interferometer, consisting of two parallel, partially reflecting plane plates, is a high-resolution multiple-beam interferometer usually used in a high order (5000 to 50,000). The theory of the Fabry-Perot interferometer and the usual conditions of its use are explained well by Meissner[24], Candler[25], and Steel[26]. The intensity distribution of the circular fringes is called the Airy distribution and is derived in any standard text in optics. A sample ray is shown in Figure 4 as it traverses the instrument, undergoing many reflections between the plates. Light of wavelength λ is incident at angle ϕ, and the plates are separated by a distance t. The optical path difference between successive outcoming rays is $2nt \cos \phi$, and constructive interference will occur along a cone with constant ϕ if this optical path is an integral multiple of the vacuum wavelength. That is, when

$$m\lambda = 2nt \cos \phi. \qquad (3)$$

Assume the intensity of light incident on the interferometer is I_o, and call the reflection coefficient R, the transmission coefficient T. Then the transmitted intensity is given by the Airy function:

$$I = I_o T^2/(1+R^2 - 2R \cos \theta) \qquad (4)$$

where θ is the phase difference, $\theta = 2\pi m$. If m is an integer, the transmitted intensity will be maximum:

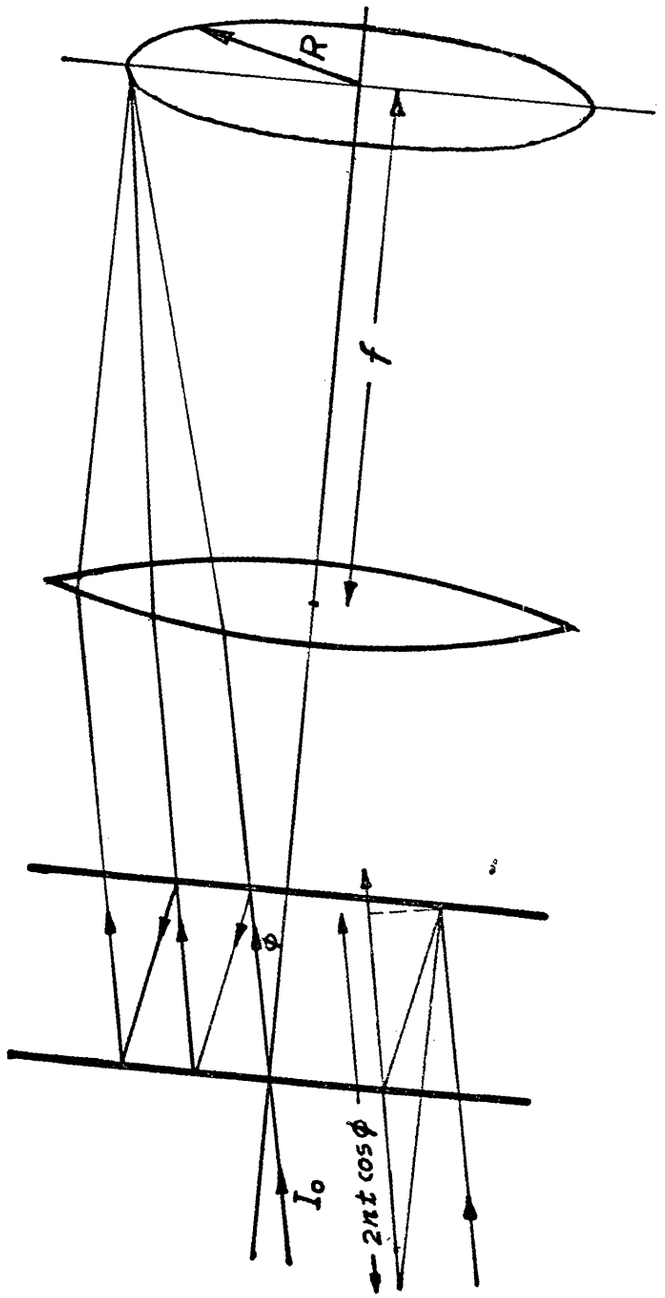

FIG.4 Fabry-Perot Interferometer

$$I_{max} = I_o T^2 / (1-R)^2, \qquad (5)$$

while half an order away from this position the intensity minimum does not go to 0:

$$I_{min} = I_o T^2 / (1+R)^2. \qquad (6)$$

The Airy function is plotted in Figure 5 for various values of the reflection coefficient R. It is clear that a higher reflection coefficient gives narrower fringes, and hence less overlap between neighboring spectral lines. In addition, with higher reflection coefficient, the constrast between maximum and minimum intensity is greater. If there is no absorption in the reflecting films, T=1-R, and the maximum intensity coming out of the instrument is equal to that going in. In practice, some light is absorbed by the reflecting surface, and the plates are coated to give about 10% overall transmission. By raising the reflection coefficient the lines can be further narrowed, but the signal to the photocell will be reduced, and the amplification system will have to be operated with longer time constant so that measurement time will be increased. It is not possible to obtain "perfectly" flat plates on which to coat the reflector. The lack of flatness will blur the spectrum merely by geometric change of the spacing t, and this puts a maximum on the reflection coefficient which would be useful. Very high reflection coeffcients can be obtained by coating the plates with alternate layers of high and low refractive index, but these high reflectance dielectric coated plates must be prepared specially for each small wavelength region requiring much work and expense to use them on more than a single line.

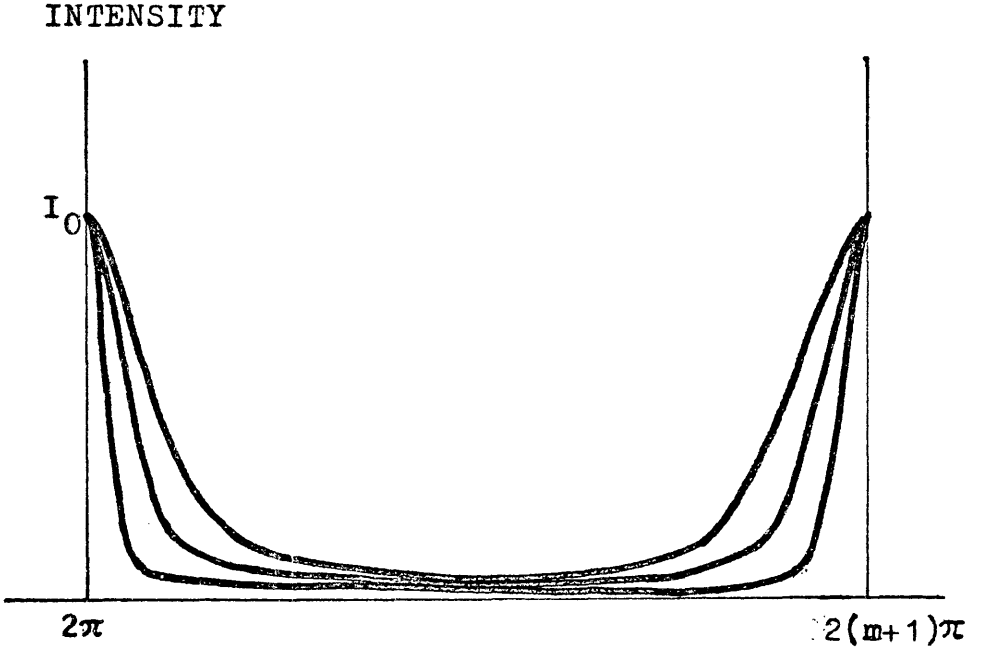

FIG. 5 Airy function plot against phase diffenence θ

The spectrum can be scanned by varying 1) the angle of incidence ϕ, 2) the refractive index of the medium between the plates, n, 3) by changing the spacing t. The first method is the one used normally with photographic recording of the spectrum, preferably evacuating the interferometer to fix n=1 exactly. Humphreys[27] has used this method with a photocell in the near infrared, tilting the interferometer to achieve scanning. This is an undesirable method for use with a photocell, since the area of each order is about the same, while the varying radius of the ring makes it almost impossible to put more than a small fraction of the order on the photocell at one time. For this reason it is important to use the central zone of the interference pattern, and scan by method 2 or 3.

Scanning by varying the pressure of the gas between the plates, and hence the refractive index, was first done by Jacquinot[28]. It permits use of a fixed spacer, so that it is easy to keep accurate knowledge of the spacing t. However, in the near infrared the refractive index of the gas used is usually not well known, and enters into the result for absolute wavelength measurements, giving a large uncertainty.

The original work of Fabry and Perot[29] in developing their interferometer was done using visual observation of the patterns, making adjustments of parallelism and spacing by small rubber sacs

filled with water under varying pressure. Besides the mechanical method used in the present work, electrostriction is often used today to give small changes in parallelism and spacing, much as in the original method, but these have a rather limited length of scan.

I-2.2 APPLICATIONS IN THE INFRARED

The first work on infrared interferometry was done by Paschen[30] and his student Ignatieff[31], using variable spacing, and looking at the central zone of the pattern with thermocouples. They measured both He 1 μ and 2 μ lines. Since the development of sensitive photoconductive cells, weaker lines can be measured and precision increased in this kind of work. Rao[32], Jaffe and Rank[33,34,35] measured molecular specra using the Fabry-Perot interferometer to improve their absolute wavelength accuracy. With the development of experimental techniques and infrared materials, the instrument will certainly be used in longer wavelength regions.[36,37]

II. ZEEMAN EFFECT OF HELIUM INFRARED LINES

II-1. THE SPECTRUM OF HELIUM

The two electrons in the helium atom have very strong coupling of their spins, resulting in spin for the atom of either S=0 or S=1. There are no lines which result from interaction of these two cases, which led early workers to postulate two distinct kinds of helium, parahelium for S=0 and orthohelium for S=1. When both electrons are in their lowest state, $n_1=n_2=1$, the Pauli exclusion principle forces them to have opposite spin, so the ground state is $(1s)^2\ {}^1S_0$. With different principal quantum numbers the spins can be equal, giving for example 1s 2s $^3S_1$, the lowest triplet excited state. All such levels with $L\neq 0$ have three fine structure terms. Within any set terms with fixed n, the energy decreases with L, and the triplet states have lower energy than the corresponding singlet states, in agreement with Hund's rules.

For both triplet and singlet term values, 2S is below 2P, and the selection rules prohibit either transition 2S to 1S[38], so both 2S terms have greater population than normal, and are called "metastable". This corresponds to a greater lifetime, since in normal sources decay will be by mechanical collision rather than by optical transition. Because of this there is resonance brightening of the lines ending in these terms, which are the lines of

interest in this study, the 2 μ line coming from 2^1P_1 to 2^1S_0, while the 1μ line comes from the transition 2^3P_{012} to 2^3S_1 as shown in Figure 6. It is worth noting that this overpopulation of the 2S levels provides the population inversion used by the He-Ne gas laser.

The life time of the 2^3P states is 0.97×10^{-7} sec, while that for the ^3S level is very long[39]. The high population in the 2S states permits both the 1μ and 2μ lines to appear in the absorption spectrum, and the very high transition probabilities cause heavy self absorption. Thus a great deal of care must be taken to avoid this effect, which has given rise to many erroneous results.

Since the interaction energy due to spin of the two electrons is large, the 2^3P forms an irregular triplet, Figure 7. Although not of particular interest here, the 3^3P terms share this property. Because the separation of the $^3P_1$ from the $^3P_2$ is so small, it is extremely hard to measure, and it was actually thought for many years that orthohelium had a doublet spectrum. While the experimental values of various workers are in good agreement, there is still not an accurate theoretical calculation of the fine structure splitting. The situation is summarized by Lamb[40]. It is clear that the 2^3P and 3^3P terms do not obey Lande's interval rule which predicts a 2:1 separation of the terms.

II-2 THEORY OF ZEEMAN EFFECT

II-2.1 BASIC THEORY

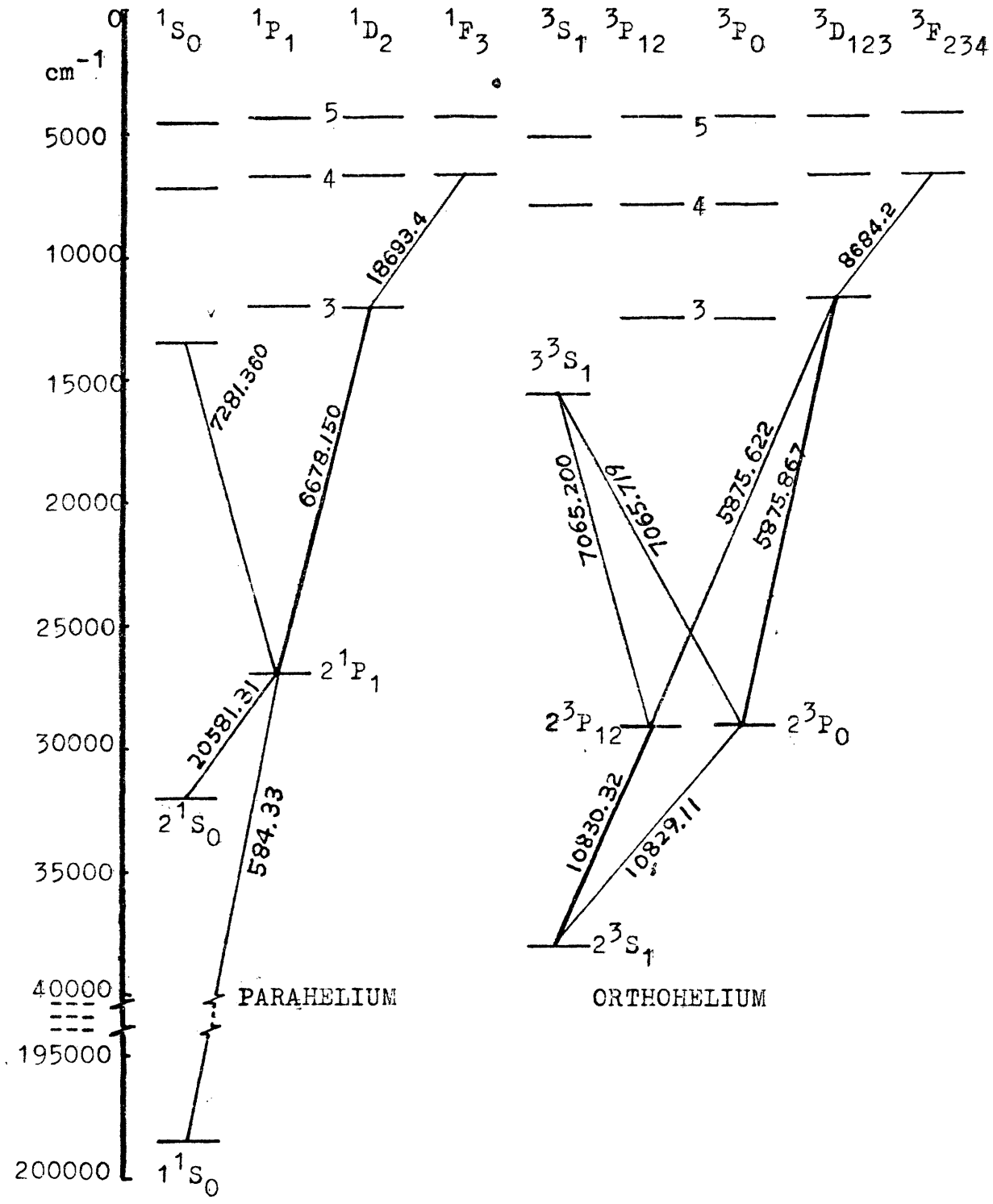

FIG. 6 Helium energy levels

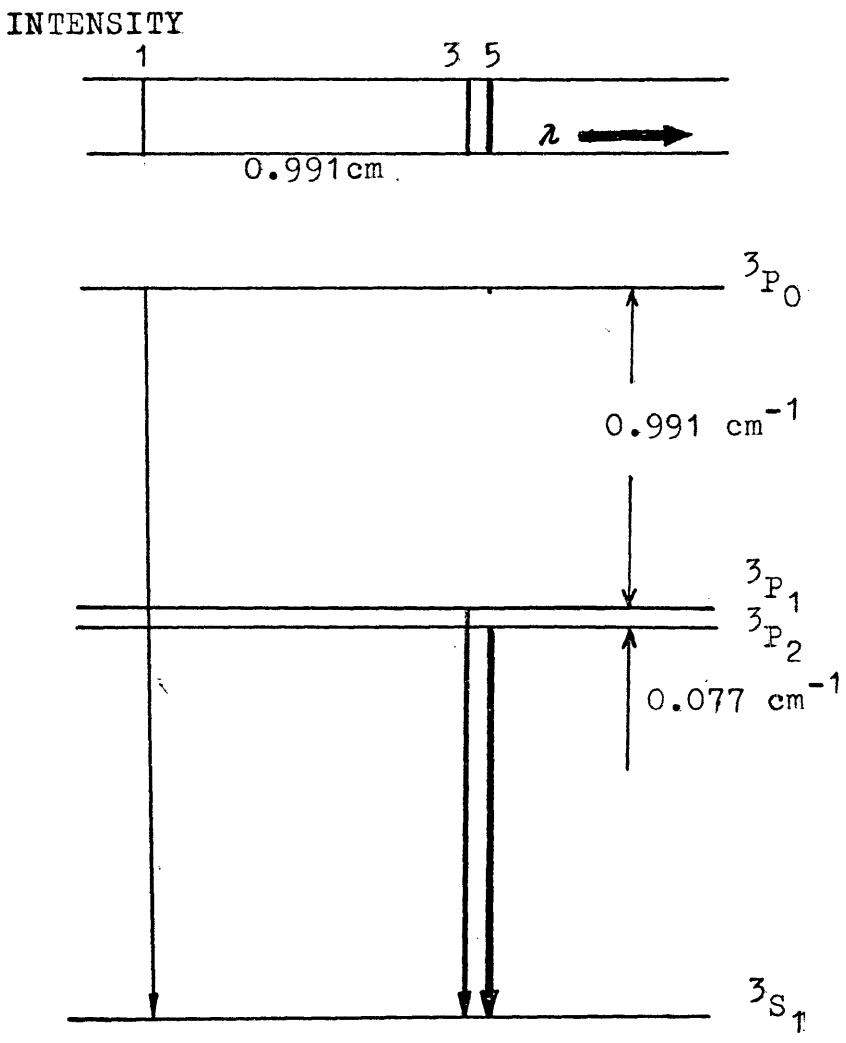

Fig.7. Fine structure of $2^3P_{012} - 2^3S_1$

At the semi-classical level of Bohr theory, the angular momentum of an electron in an orbit and the magnetic moment of that electron are proportional, and are given by the same quantum number. Thus the quantization of angular momentum in multiples of $\hbar$ gives rise automatically to quantization of magnetic moment, which turns out to have smallest value $\mu_B = 4\mu_B = e\hbar/2mc$, called the Bohr Magneton. The selection rule $\Delta L = \pm 1$ would then give rise to triplet spectra with spacing proportional to the magnetic field causing the change of energy. When lines were found which fulfilled this prediction, they were labelled Normal Zeeman Effect, but most lines do not fulfill these conditions, hence were labelled Anomalous Zeeman Effect. In 1925 Uhlenbeck and Goudsmit[41] postulated the presence of electron spin to account for fine structure and it was immediately found that the angular momentum $\hbar/2$ and magnetic moment of one Bohr magneton would account for the observed results. This factor of two between the quantum number for mechanical effect and magnetic effect was soon calculated by Dirac using relativistic wave mechanics. It is known as the gyromagnetic ratio, with limiting values g=1 for pure orbit and g=2 for pure spin.

In Russell-Saunders coupling, which is valid for light atoms, the total angular momentum vector for the atom, L, couples with the total spin momentum vector, S, to form a total angular momentum vector J. When the gyromagnetic ratio for spin is put into this vector model, Figure 8 results. From the figure the law of cosines gives $L^2 = J^2 + S^2 - 2JS \cos \theta$, and $S^2 = J^2 + L^2 - 2JL \cos \phi$. When the double spin vector is included, the resultant instantaneous magnetic moment is no longer parallel to Jh. However, there is no inertia

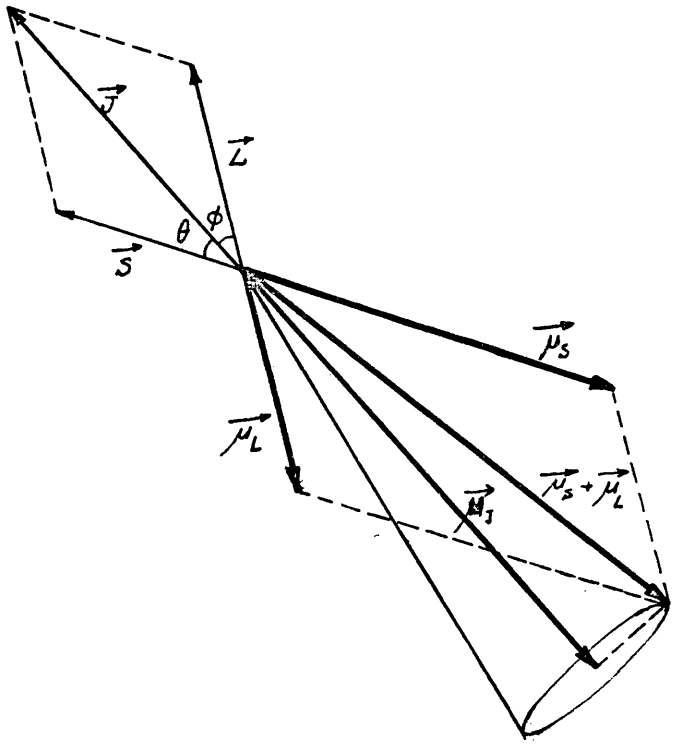

Fig.8 Vector model for spin and orbit magnetic moment

preventing precession about the line of Jh, so this happens very rapidly, giving an effective magnetic moment equal to the J component of the instantaneous value. This is:

$$\mu_J=(L\cos\theta + 2S\cos\phi)\mu_B = J\left[(3J^2+S^2-L^2)/2J^2\right]\mu_B \qquad (7)$$

where μ_B is the value of the Bohr magneton, and the qunatity in brackets is the desired general expression for the gyromagnetic ratio in the presence of both orbit and spin magnetic moment. It would be surprising if this simple derivation gave an exact result, and it does not, but it seems even more surprising that Lande was able to find the correct result empirically before the first publication of wavemechanics, replacing the square of each vector with that vector times a number one greater:

$$g = 1+\frac{J(J+1)+S(S+1)-L(L+1)}{2J(J+1)} \qquad (8)$$

It is easy to check that the correct values come out of this expression when L=0 or S=0. In a few states both S and L are zero giving an indeterminate result, but this is of no consequence, since there is then no magnetic moment to calculate.

With this magnetic moment in a magnetic field H, the interaction energy is given by

$$E = gJH\mu_B\cos(H,J) = gm\mu_B H \qquad (9)$$

where m is the magnetic quantum number for the atom, giving the quantized component of J which is parallel to the magnetic field,

and (H,J) is the angle between H and J. Dividing equation (9) by hc, and introducing the Lorentz unit $\mathcal{L} = \frac{He}{4\ meC^2} = \mu_o H$, we have the interaction energy in wavenumbers

$$\Delta(1/\lambda) = gm\mathcal{L} \tag{10}$$

II-2.2 SELECTION RULES AND INTENSITY RULES (WEAK FIELD)

The allowable transitions between terms are those where magnetic quantum number changes by 1, 0, or -1, namely, $\Delta m = 0, +1, -1$. The polarization of the Zeeman lines depends on the direction of view and also depends on the Δm . It may be stated as:

1) viewed perpendicular to the field

$\Delta m = +1, -1$	plane polarized perpendicular to field, s component	(11)
$\Delta m = 0$	plane polarized parallel to field, p component	

2) viewed parallel to the field

$\Delta m = +1, -1$	circularly polarized, s component	
$\Delta m = 0$	forbidden	(12)

When the states are in thermal equalibrium, the sum of intensities of the lines having a common upper or lower state is proportional to $2j + 1$ of that state[42]. Therefore, the ratio of the intensity sum for lines from level of j_1 to that from level of j_2 is

$$\frac{I_2}{I_1} = \frac{2j_2 + 1}{2j_1 + 1} \tag{13}$$

From this sum rule, Ornstein and Burger[43] derive the intensity rules for the Zeeman levels in a weak magnetic field. (For the intensity rules, see also in White[44]). The intensity rules can be stated as follows: the sum of the intensities of all the transitions starting from any initial Zeeman level is equal to the sum for all transitions starting from any other level. Similarly, the sum of the intensities of all the transitions arriving at any final Zeeman level is equal to the sum of intensities of those arriving at any other level. Briefly, the intensity can be determined from the following formulas:

$$\Delta j = 0:$$

$$m \rightarrow m \pm 1 \qquad I = A(j \pm m + 1)(j \pm m)$$

$$m \rightarrow m \qquad I = 4Am^2 \tag{14}$$

$$\Delta j = \pm 1:$$

$$m \rightarrow m \pm 1 \qquad I = B(j \pm m + 1)(j \pm 2)$$

$$m \rightarrow m \qquad I = 4B\,(j + m + 1)\,(j - m + 1) \tag{15}$$

where A and B are proportional constants.

II-2.3 CALCULATION OF ZEEMAN PATTERN (WEAK FIELD)

A rapid way to use the g factor and the selection rules to predict the Zeeman pattern is shown in Table 1. The m values are written in the top row. Below each value of m, gm values of initial and final states are filled in. The arrows indicate transitions which obey the selection rules. The vertical differences are p components, the diagonal differences are the s components.

m	-j	-(j-1)	----	j+1	j
$mg_{initial}$	$-j \cdot g_i$	$-(j-1)g_i$	----	$(j+1)g_i$	$j \cdot g_i$
transitions					
mg_{final}	$-j \cdot g_f$	$-(j-1)g_f$	----	$(j+1)g_f$	$j \cdot g_f$

Table 1. Calculations of Zeeman Patterns

As a demonstration of using this table, the Zeeman splitting of $^3P_2 - {}^3_1S_1$ transition is predicted as follows. For the $^3P_2$ level $g=1+\frac{2\cdot3+1\cdot2-1\cdot2}{2\cdot2\cdot3}=\frac{3}{2}$ by Equation 8 while the $^3S_1$ level has $g=1+\frac{1\cdot2+1\cdot2-0\cdot1}{2\cdot1\cdot2}=\frac{4}{2}$. The calculation is then tabulated as:

m	2	1	0	-1	-2
mg ($^3P_2$, $g=\frac{3}{2}$)	$\frac{6}{2}$	$\frac{3}{2}$	0	$-\frac{3}{2}$	$-\frac{6}{2}$
mg ($^3_1S_1 g=\frac{4}{2}$)		$\frac{4}{2}$	0	$-\frac{4}{2}$	

Transitions for s components: $\frac{6}{2} \to \frac{4}{2}$, $\frac{3}{2} \to 0$, $0 \to \frac{4}{2}$

Transitions for p components: $\frac{3}{2} \to \frac{4}{2}$, $0 \to 0$

So the Zeeman Splitting of this particular transition is

$$\Delta\left(\frac{1}{\lambda}\right) = \pm (0,4)\ 2,3,4_{0} \quad /2\,\mathcal{L} \tag{16}$$

in the usual shorthand notation:

Kiess and Meggers have given a very useful intensity rule[44]. If the j values of the coupling terms are not equal, the vertical differences in the middle of the table and the diagonal differences at the ends given the strongest p and s component respectively. If the j values are equal, the vertical differences at the ends of the table and the diagonal differences in the middle give the strongest p and s component respectively. For terms of odd multiplicity, the p component of transition M=0 to M=0 is forbidden, i.e. the intensity is zero.

II-2.4 ZEEMAN EFFECT FOR STRONG FIELD

For a very strong magnetic field, the coupling mechanism between all the L and S are broken down with L and S precessing independently around the field direction. j is no longer a valid quantum number. This is called complete Paschen-Back effect. The spectral lines have the appearance of a Lorentz triplet, so it may be designated quasi-normal Zeeman effect. This occurs when the Zeeman split is greater than the fine structure splitting. White[45] has a detailed discussion for the strong field case.

II-2.5 ZEEMAN EFFECT FOR INTERMEDIATE FIELD STRENGTH

The calculation of Zeeman pattern is simple for the cases of weak field and strong field. When the Zeeman splitting is comparable with the fine structure term, the situation is more difficult. Quantum mechanics has to be used to calculate the splitting terms and the line intensities.

In a magnetic field H, the atom can be described by the Hamiltonian[45,40]:

$$\mathcal{H} = \mathcal{H}_0 + \mathcal{H}_m \qquad (17)$$

where $\mathcal{H}_0$ represents the fine structure interaction, $\mathcal{H}_m$ is the magnetic perturbation which represents the interaction of the magnetic field with the electron spin and orbital motion. In the case of intermediate field strength, we have to find the exact eigen value due to the perturbed Hamiltonian $\mathcal{H}_m$ because the interaction energy of spin-coupling is about of the same order of $\mathcal{H}_m$ and $m=m_L+m_S$ is a constant of motion in the whole region. The states of the same m are intermixed. In the jm configuration[46,45], the eigen-values E of these states can be determined from the matrix $(j'm' \mid \mathcal{H} \mid jm)$ and is the solution of the secular equation:[45,47,48]

$$\begin{vmatrix} (\mathcal{H}_m)_{L+S,L-S} + E_{L+S} - E & (\mathcal{H}_m)_{L+S,L+S-1} \cdots (\mathcal{H}_m)_{L+S,1L-S} \\ (\mathcal{H}_m)_{L+S-1,\,L+S} & (\mathcal{H}_m)_{\substack{L+S-1 \\ L+S-1}} + E_{L+S-1} - E \cdots\cdots \\ (\mathcal{H}_m)_{L-S\,,L+S} & \cdots \qquad\qquad \cdots\cdots\cdots \end{vmatrix} = 0 \qquad (18)$$

ARTHUR LAKES LIBRARY
COLORADO SCHOOL of MINES
COLORADO 80401

In this equation, $(\mathcal{H}_m)_{j,j'}$ is the matrix element of the external perturbationenergy between state j and j', E_J is the fine structure energy of the state j without external field. This method for Zeeman effect in an intermediate field strength will be used in Section II-3.2.

II-3 THE ZEEMAN EFFECT OF HELIUM

The Zeeman effect of the helium spectrum has been observed by many workers.[49,50,51,52] In 1906, Lohmann found that the theory is in good agreement with the experiment for the singlet lines 6678, 5048, 5016, and 4922 Å. A theoretical splitting of He 1μ was given by Bethe[47]. The Paschen-Back effect of the 3^3D-2^3P lines (5876Å) in a field of 9500 Gauss was measured in 1928.[48] More Zeeman effects of helium lines and the combination of Zeeman and Stark effect[51,52] has been studied.

II-3.1 THE ZEEMAN EFFECT OF PARA-HELIUM SINGLET

The parahelium singlet has a normal Zeeman effect. Because S=0, there is no spin-orbit coupling term and the energy shift is linear with the field. Quantum mechanically speaking, the field-free wave function is the exact eigen-function at all values of field strength. As an example for the Zeeman effect in the singlet system, the He 2μ line was chosen and measured.

This line results from the transition $2^1P_1 - 2^1S_0$. The components of its Zeeman pattern can be easily obtained by using Table 1

with g=1 for S=0. Equation (15) can be used for the intensities of the components. From Equation (10), we have

$$\Delta\left(\frac{1}{\lambda}\right) = \pm \alpha \ (\text{cm}^{-1}) = 4.674 \times 10^{-5} H \ (\text{cm}^{-1}) \qquad (19)$$

For an external field H, the Zeeman splitting is shown in Figure 9. With H = 5200 Gauss, the expected shift is $\Delta\left(\frac{1}{\lambda}\right) = 0.243 \ \text{cm}^{-1}$ and

$$\Delta\lambda = \lambda^2 \cdot 0.243 = 1.029 \ \text{Å} \qquad (20)$$

II-3.2 ZEEMAN EFFECT OF ORTHO-HELIUM TRIPLET

For the triplet states of the ortho-helium system the situation is more complicated. For L = 0 states (^{3}S terms), the field-free wave function of m = 1, 0, -1 is the exact eigenfunction and the state split into three levels with interval of $\pm 2\mu_0 H$. For the state of L > 1 (D, F, ···terms), the separations of the original multiplet is very small. For example, $^3D_1 - {}^3D_2$: 0.02 cm^{-1}; $^3D_2 - {}^3D_3$: 0.06 cm^{-1} (See Keesom[48]). So even a weak field has $\mu_0 H$ much larger than the fine structure splitting and therefore complete Paschen-Back effect occurs.

For the states of L = 1, (the ^{3}P state), the separation between $^3P_2$ and $^3P_1$ is also small but the separation between $^3P_1$ and $^3P_0$ is comparable with $\mu_0 H$ (see Figure 7 for fine structure of 2^3P state). The six state of m = ±1, ± 2 from $^3P_2$ and $^3P_1$ terms have a complete Paschen-Back effect and therefore show normal Lorentz triplet.

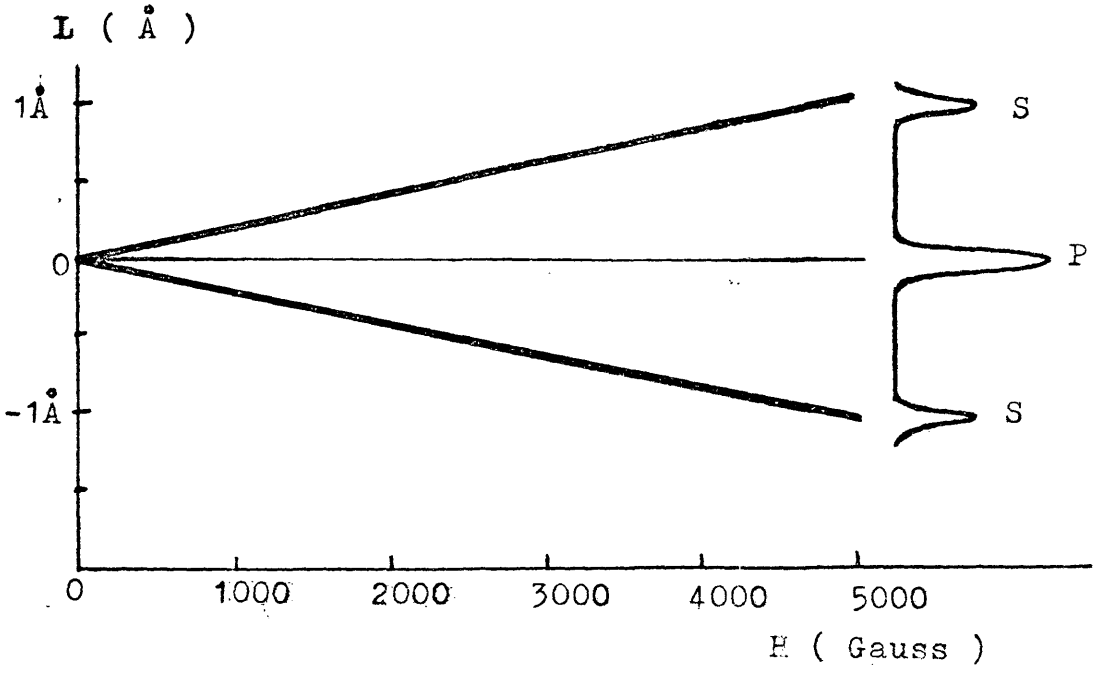

Fig.9 ZEEMAN SPLITTING OF HELIUM 2 μ LINE

Now, as a good example for Zeeman effect for the ortho-helium triplet system we will calculate the splitting of the He 1μ line which belongs to the third case of L = 1. Using a permanent magnet of 5200 Gauss, we were able to obtain $\mu_0 H$ of 0.243 cm^{-1} (equation (19)) which is larger then $E_2-E_1 = 0.077\ cm^{-1}$ but smaller than $E_1-E_0=0.99\ cm^{-1}$. So the method discussed in Section II-2.5 will be used. Working with the jm configuration with Russell-Saunder eigen-function (see Condon and Shortley[46], Chapter III), the eigen-value can be obtained from the matrix $(j'm'|\mathcal{H}|jm)$.

II-3.2.1 The m=0 states: there are the combinations of m_L, m_S= 1,-1;0.0;-1,1. Without an external field, the coefficients of the eigen-function $\Psi(jm)$ are the Clebsch-Gordan coefficients which are shown in Table 2.

	$m_L=1$	$m_L=0$	$m_L=-1$
j=0	$\left[\frac{(1-m)(2-m)}{6}\right]^{\frac{1}{2}}$	$-\left[\frac{(1-m)(1+m)}{3}\right]^{\frac{1}{2}}$	$\left[\frac{(2+m)(1+m)}{6}\right]^{\frac{1}{2}}$
j=1	$-\left[\frac{(1+m)(2-m)}{4}\right]^{\frac{1}{2}}$	$\left(\frac{m}{2}\right)^{\frac{1}{2}}$	$\left[\frac{(1-m)(2+m)}{4}\right]^{\frac{1}{2}}$
j=2	$\left[\frac{(1+m)(2+m)}{12}\right]^{\frac{1}{2}}$	$\left[\frac{(2+m)(2-m)}{6}\right]^{\frac{1}{2}}$	$\left[\frac{(2-m)(1-m)}{12}\right]^{\frac{1}{2}}$

Table 2. The Clebsch-Gordan Coefficient

So for these m=0 states, the coefficients are

m_L, m_S	1,-1	0,0	-1,1
j=0	$\frac{1}{\sqrt{3}}$	$-\frac{1}{\sqrt{3}}$	$\frac{1}{\sqrt{3}}$
j=1	$-\frac{1}{\sqrt{2}}$	0	$\frac{1}{\sqrt{2}}$
j=2	$\frac{1}{\sqrt{6}}$	$\frac{2}{\sqrt{6}}$	$\frac{1}{\sqrt{6}}$

Then the matrix becomes

$$(j'0 \mid \mathcal{H} \mid j\ 0) = \begin{bmatrix} E_0 & \sqrt{\frac{2}{3}}\mu_0 H & 0 \\ \sqrt{\frac{2}{3}}\mu_0 H & E_1 & \sqrt{\frac{1}{3}}\mu_0 H \\ 0 & \sqrt{\frac{1}{3}}\mu_0 H & E_2 \end{bmatrix} \tag{21}$$

With the permanent magnet of 5200 Gauss, $\mu_0 H = 0.243\ cm^{-1}$, we have $E_0-E_1 > H > E_2-E_1$ $(0.991 > 0.243 > 0.077)$. The approximation gives the eigen values (Lamb[43] has the exact form of the secular equation):

$$E_a = E_0 + \frac{2}{3}\frac{(\mu_0 H)^2}{E_0-E_1} \tag{22}$$

$$E_b = \tfrac{1}{2}(E_1+E_2) - \frac{1}{3}\frac{(\mu_0 H)^2}{E_0-E_1} + \sqrt{\tfrac{1}{3}}\ u\ H \tag{23}$$

$$E_c = \tfrac{1}{2}(E_1+E_2) - \frac{1}{3}\frac{(\mu_0 H)^2}{E_0-E_1} - \sqrt{\tfrac{1}{3}}\ u\ H \tag{24}$$

Put the numerical values of E_1, E_2, E_0 and $\mu_0 H$ $(0.243\ cm^{-1})$ into the above two equations yielding:

$$E_a = E_0 + 0.0397\ cm^{-1} \tag{25}$$

$$E_b = \tfrac{1}{2}(E_1+E_2) + 0.120\ \text{cm}^{-1} \tag{26}$$

$$E_c = \tfrac{1}{2}(E_1+E_2) - 0.16\ \text{cm}^{-1} \tag{27}$$

The three m=0 states E_a, E_b, and E_c are shown in Figure 8 with a=0.0397 cm^{-1}, b=0.120 cm^{-1}, and c=0.16 cm^{-1}.

II-3.2.2 For the m = $\pm$ 1 states which come from j=1 and j=2 terms. There are combination of m_L, m_S=0.1; 1,0; 0,-1; -1,0. The matrix for m=$\pm$ 1 is

$$(j'\pm 1|H|j\pm 1) = \begin{bmatrix} E_{1\pm\frac{3}{2}}\mu_o H & \frac{1}{2}\mu_o H \\ \frac{1}{2}\mu_o H & E_{0\pm\frac{3}{2}}\mu_o H \end{bmatrix} \tag{28}$$

So the eigen values for j=1 and j=2 are

$$E(1,\pm 1) = \tfrac{1}{2}(E_1+E_2) \pm \tfrac{3}{2}\mu_o H + \tfrac{1}{2}\left[(E_1-E_2)^2 + (\mu_o H)\right]^{\frac{1}{2}} \tag{29}$$

$$E(2,\pm 1) = \tfrac{1}{2}(E_1+E_2) \pm \tfrac{3}{2}\mu_o H - \tfrac{1}{2}\left[(E_1-E_2)^2 + (\mu_o H)\right]^{\frac{1}{2}} \tag{30}$$

Clearly, if E_1-E_2=0, then the Zeeman splitting is four levels of equal intervals $\mu_o H$.

With numerical values, we have for H=5200 Gauss

$$E(1,+1) = \tfrac{1}{2}(E_1+E_2) + 0.492\text{cm}^{-1} (\text{or } 2.024\mu_o H) \tag{31}$$

$$E(1,-1) = \tfrac{1}{2}(E_1+E_2) - 0.237\text{cm}^{-1} (\text{or } -0.975\mu_o H) \tag{32}$$

$$E(2,1) = \tfrac{1}{2}(E_1+E_2) + 0.237\text{cm}^{-1} \tag{33}$$

$$E(2,-1) = \tfrac{1}{2}(E_1+E_2) - 0.492\text{cm}^{-1} \tag{34}$$

The four states are almost equally distributed around $\frac{1}{2}(E_1+E_2)$.

II-3.2.3 For the $m=\pm 2$ states, which come from J=2 term only. In this case, the matrix is the simplest one by one, just an element of

$$(2, \pm 2 \mid H \mid 2, \pm 2) = E_2 \pm 3 \mu_o H \qquad (35)$$

and the corresponding eigen-value is then

$$E\ (2, \pm 2) = E_2 \pm 3\ \mu_o H \qquad (36)$$

II-3.2.4 This completes the calculation of the splitting of the upper state of 1μ. For the lower state $^3s_1$, L=0, was discussed at the beginning of Section II-3.2. The upper state of $^3P_1$ in the field splits into 9 levels which combine with 3 levels of $^3S_1$. Figure 11 shows the state splitting and the allowed transitions. Six $m=\pm 1, \pm 2$ states show complete Paschen-Back effect. Six transitions are allowed from those $m=\pm 1, \pm 2$ states as governed by selection rule $M_s=0$. Transition 11 and 14 have $M_L=0$ and therefore are the p components.

II-3.2.5 As discussed in Section II-2.2, the sum of intensities of all the transitions starting from any initial Zeeman level is the same. This was proved to be true for this case by Lamb[40] by considering the dipole radiation matrix and polarization. He said "all sublevels 3p (j,m) decay to 2^3S_1 at the same rate." Considering the polarization of the Zeeman components with the observation

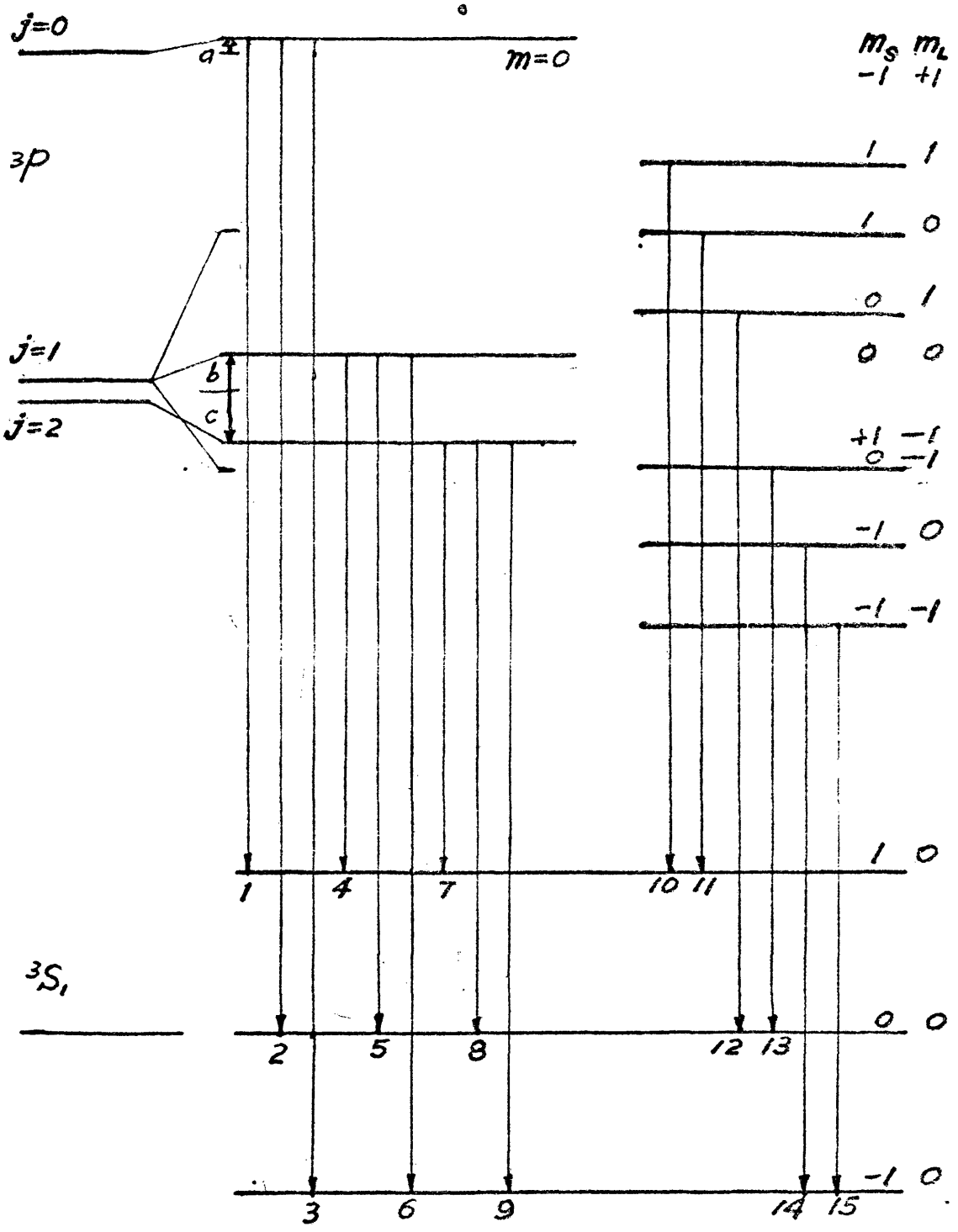

FIG.10 Zeeman Transitions of He $^3P_{012}$ - $^3S_1$

direction perpendicular to the field, intensity of transitions 11 to 15 can easily be determined as they are components of normal Lorentz triplet. Each p component (transitions 11 and 14) has twice intensity of an s component. That is

$$I_{11}=I_{14}=2I_{10}=2I_{12}=2I_{13}=2I_{15} \qquad (37)$$

To obtain intensities for the transitions from m=0 states (transitions 1 to 9), the perturbed coefficients[53,40] of the eigen-function will be used. Putting the eigen-values back into the original equation gives the relation between the coefficients. For the perturbed states (equations (22), (23) (24)), the coefficients m=0 become[47,48]

m_L, m_S	1,-1	0,0	-1,1	
E_a	$\frac{1}{\sqrt{3}}$	$-\frac{1}{\sqrt{3}}$	$\frac{1}{\sqrt{3}}$	TRANSITION 1 - 3
E_b	$\frac{1+\sqrt{3}}{2\sqrt{3}}$	$\frac{1}{\sqrt{3}}$	$\frac{1-\sqrt{3}}{2\sqrt{3}}$	4 - 6
Ec	$\frac{1-\sqrt{3}}{2\sqrt{3}}$	$\frac{1}{\sqrt{3}}$	$\frac{1+\sqrt{3}}{2\sqrt{3}}$	7 - 9

The intensities can then be determined with the help of the transition probability.[53,46] Within the m=0 states, the first field-free j=0 state (Figure 10) simply shows a normal triplet with central p component, transition 2, of twice intensity of the s component, transition 1 and 3. The intensities and also the energy splitting of equation (31), (32), (33), (34), and (36) are listed in Table 3. In this table, the intensities are normalized to a scale of 12. As there are five transitions from J=2, three

TRAN-SITION	E (μ_oH)	POLARI-ZATION	j_i	$m_i - m_f$	INTEN-SITY
1	-2+a	s	0	0 1	2
2	a	p	0	0 0	4
3	2+a	s	0	0 -1	2
4	-2+b	s	1	0 1	3.15
5	b	p	1	0 0	4
6	2+b	s	1	0 -1	0.85
7	-2-c	s	2	0 1	0.85
8	-c	p	2	0 0	4
9	2-c	s	2	0 -1	3.15
10	1	s	2	2 1	6
11	0	p	1	1 0	12
12	1	s	2	1 -1	6
13	-1	s	1	1 1	6
14	0	p	2	1 0	12
15	-1	s	2	2 -1	6

TABLE 3. Zeeman splitting of He 1u

Fig. 11

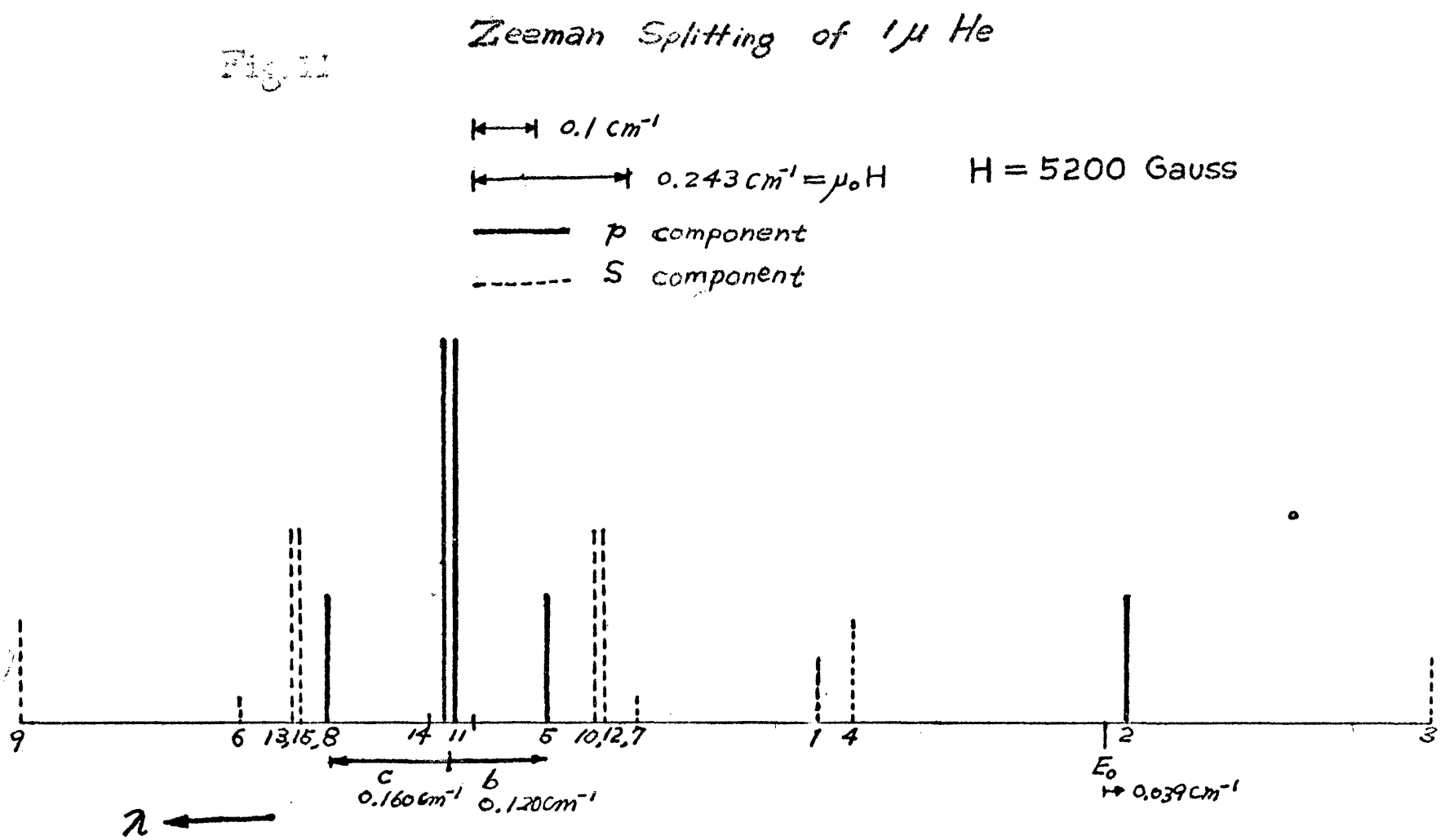
Zeeman Splitting of 1μ He
0.1 cm⁻¹
0.243 cm⁻¹ = μ₀H
H = 5200 Gauss
p component
S component
9
6
13,15,8
14
11
5
10,12,7
1
4
2
3
c
0.160 cm⁻¹
b
0.120 cm⁻¹
E₀
0.039 cm⁻¹
λ

Fig. 11

from j=1, one from j=0 so the sum rule, equation (18) is obeyed. Figure 11 shows the Zeeman pattern at H=5200 Gauss.

II-4. A REMARK ON THE CALCULATION OF ZEEMAN EFFECT

Heisenberg[54] and Darwin[55] applied quantum mechanics to calculate the standard Zeeman effect at all values of field strength. Darwin's calculation of positions and intensities of lines are found in very good agreement with some experiments.[53] Darwin's calculation for the S-P triplet is reproduced as Figure 12. In this work, the magnetic parameter $w = \frac{eHh}{4\pi m_e c}$ (Larmor frequency) is the normal Zeeman effect in energy unit. The Darwin's method is based upon the Lande's interval rule which would expect 1:2 separation for $^3P_0$-$^3P_1$-$^3P_2$. For atoms like He or Be, this does not give a reasonable result. Also Darwin's theory is satisfactory only for LS-coupling. Green[53] compares many theoretical results with his experimental results. Houston's method[57] which is not good for light atoms was also discussed.

The intensity rules for the Zeeman effect, equations (16), (17) which are derived from the classical orbit model are good for any complex spectra. White said (ref. 44, p. 289) "since these rules involve only the j's and m's of the initial and final states, they are valid for all coupling schemes." But since for strong field j ceases to be a valid quantum number (Section II-2.4) we can not use the original j in these equations.

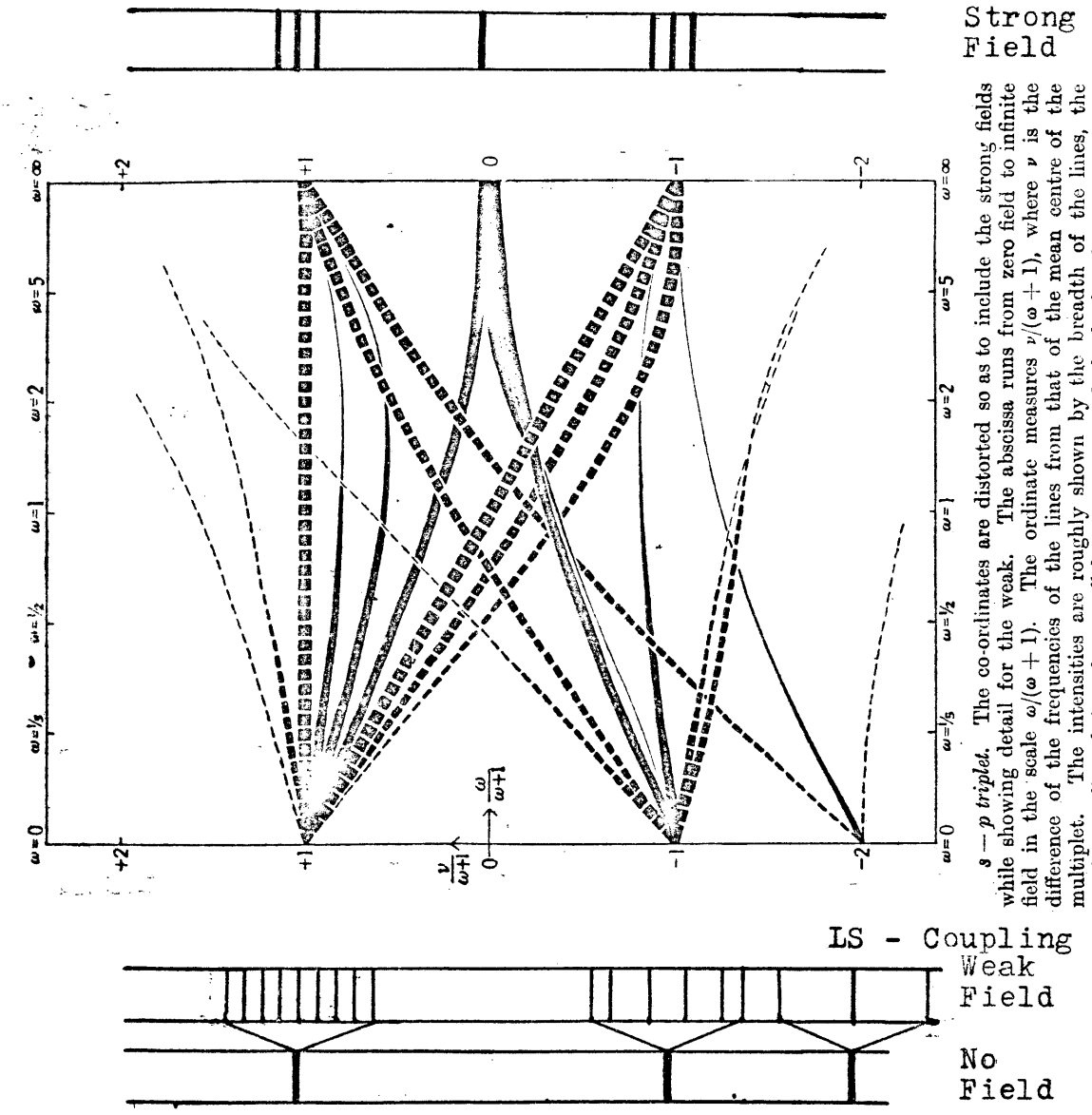

s — p triplet. The co-ordinates are distorted so as to include the strong fields while showing detail for the weak. The abscissa runs from zero field to infinite field in the scale $\omega/(\omega+1)$. The ordinate measures $\nu/(\omega+1)$, where ν is the difference of the frequencies of the lines from that of the mean centre of the multiplet. The intensities are roughly shown by the breadth of the lines, the continuous lines being the parallel components and the broken lines the perpendicular components.

Fig. 12 Darwin's calculation for S-P triplet . Zeeman effect at all field strength.

II-4.1 THE ZEEMAN EFFECT OF He 1μ AT VERY WEAK FIELD

Under a very weak field of $\mu_o H \ll 0.077\ cm^{-1}$ $(=E_2-E_1)$. Paschen-Back effect will not occur for He 1μ lines. The Zeeman splitting can be easily calculated by the method shown in the example in Section II-2.3. Figure 13 shows the possible transitions between the split energy levels. (Each transition here is labeled with a prime (') to distinguish from those discussed before.) Transition 5' is forbidden by the section rule and its intensity is zero.

Using equations (16) and (17) we get the intensities for each transition as listed in the Table 4. The constants A and B are needed because only the relative intensities are of interest. From the sum rules stated in equation (15):

$$\sum I_{\substack{\text{transition } 1'\text{-}3' \\ \text{(same upper state)}}} : \sum I_{(4'\text{-}10')} : \sum I_{(11'\text{-}19')}$$

$$= 1 : 3 : 5. \qquad (38)$$

But from the listed individual intensities

$$\sum I_{(1'\text{-}3')} : \sum I_{(4'\text{-}10')} : \sum I_{(11'\text{-}19')}$$

$$= 8 : 16 : 80 = \tfrac{1}{2} : 1 : 5.$$

Therefore the intensity value of each transition is found by multiplying the intensity value for transition 1', 2', 3' by two and those of 4' through 10' by three. In Table 4, we summarized the relative intensities and the line positions which can be compared with Darwin's result for weak field.

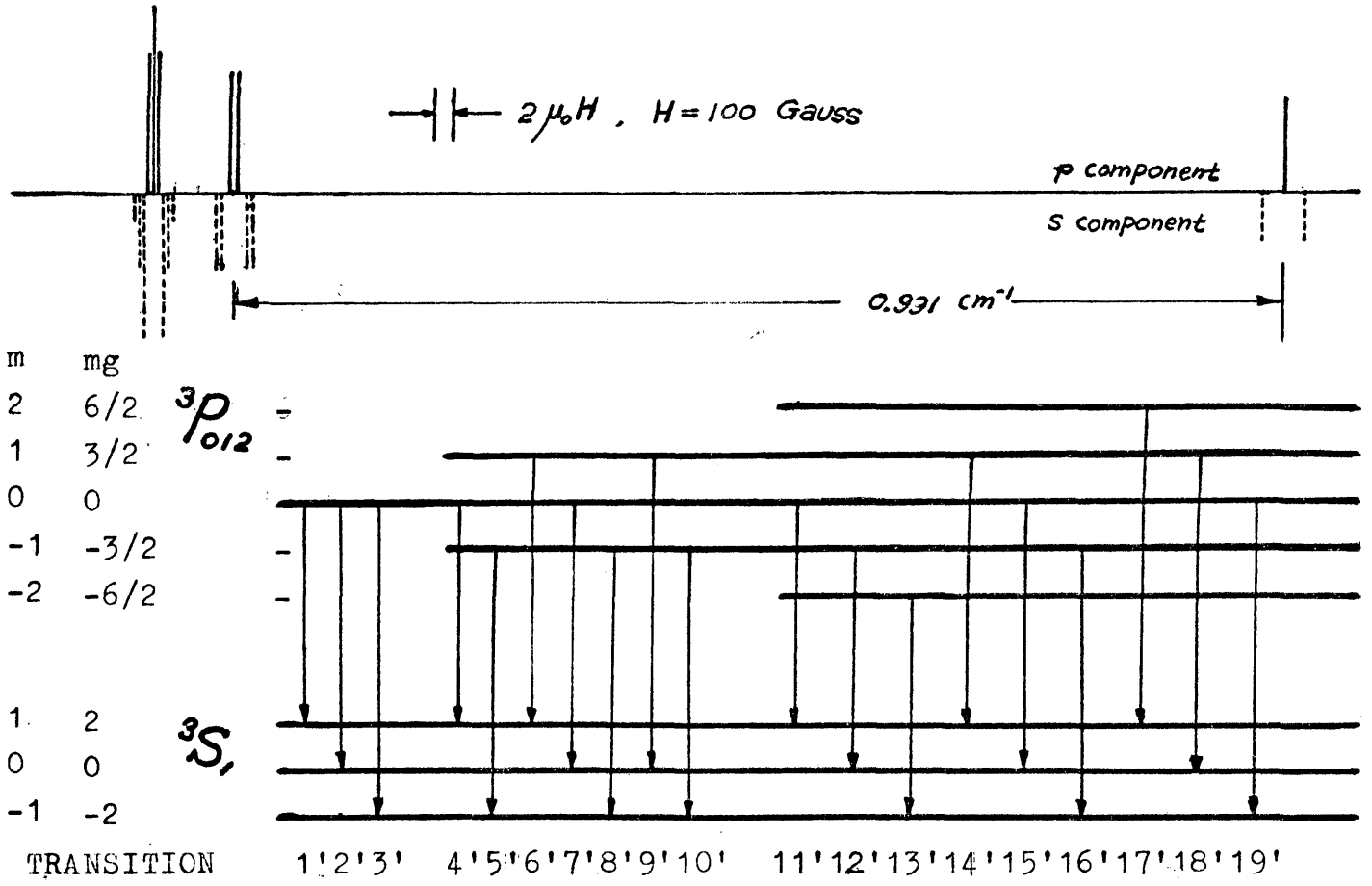

Fig.13 $^3P_{012}$-$^3S_1$ Zeeman Splitting Under Very Weak Field

TRANSITION	j_i	j_f	m_i	m_f	POLARITY	INTENSITY VALUE	RELATIVE INTENSITY	POSITION (in $\mathcal{L}$)
1'	0	1	0	1	s	$I_1 = 2B$	4	2
2'			0	0	p	$I_2 = 4B$	8	0
3'			0	-1	s	$I_3 = 2B$	4	-2
4'	1	1	0	1	s	$I_4 = 2A$	6	2
5'			-1	0	s	$I_5 = 2A$	6	3/2
6'			1	1	p	$I_6 = 4A$	12	1/2
7'			0	0	p	$I_7 = 0$	0	0
8'			-1	-1	p	$I_8 = 4A$	12	-1/2
9'			1	0	s	$I_9 = 2A$	6	-3/2
10'			0	-1	s	$I_{10} = 2A$	6	-2
11'	2	1	0	1	s	$I_{11} = 2B$	2	2
12'			-1	0	s	$I_{12} = 6B$	6	3/2
13'			-2	-1	s	$I_{13} = 12B$	12	1
14'			1	1	p	$I_{14} = 12B$	12	1/2
15'			0	0	p	$I_{15} = 16B$	16	0
16'			-1	-1	p	$I_{16} = 12B$	12	-1/2
17'			2	1	s	$I_{17} = 12B$	12	-1
18'			1	0	s	$I_{18} = 6B$	6	-3/2
19'			0	-1	s	$I_{19} = 2B$	2	-2

TABLE 4. ZEEMAN SPLITTING OF He 1u AT VERY WEAK FIELD

There are so many lines in a small region of $\pm 2\mathcal{L}$ with $\mathcal{L} \ll 0.077\ cm^{-1}$, so it is impossible to resolve them by traditional optical methods. (For example, 9 lines for $2^3P_2 - 2^3S_1$, the energy difference between any two of them is only $\frac{1}{2}\mathcal{L}$). Lamb[40] used the method of RF resonance to study the transitions between the Zeeman levels and calculate the actual positions of the original lines under no external field.

III. DESCRIPTION OF THE EQUIPMENT

III-1 THE OPTICAL SYSTEM

III-1.1 CONSTRUCTION OF FABRY-PEROT INTERFEROMETER

The variable spacing interferometer was built by John V. Kline at Purdue University and is described in his thesis[57]. A brief summary will be given here for completeness.

Two interferometer plates were mounted on a parallelogram, one on the top and the other on the bottom as shown in Figure 14. The plates can be made parallel to each other by adjusting the screws at A and B.

Originally magetostriction was used to produce smooth and fine motion of a plate. Now thermal expansion of a nickel rod mounted on the top of the parallelogram moves the plate. The rod is linked to a micrometer head which is fixed on the housing of the parallelogram. A solenoid of copper tube surrounds the nickel rod, Figure 15, heating the water in the tube; it will change the length of the rod to produce variable spacing. Because the temperature of the circulating water is critical, an automatic temperature control system is used. Changing the voltage across the heating coil in that system permits changing the speed of scanning.

III-1.2 THE SPECTROMETER

The structure of the optical system is shown in Figure 16.

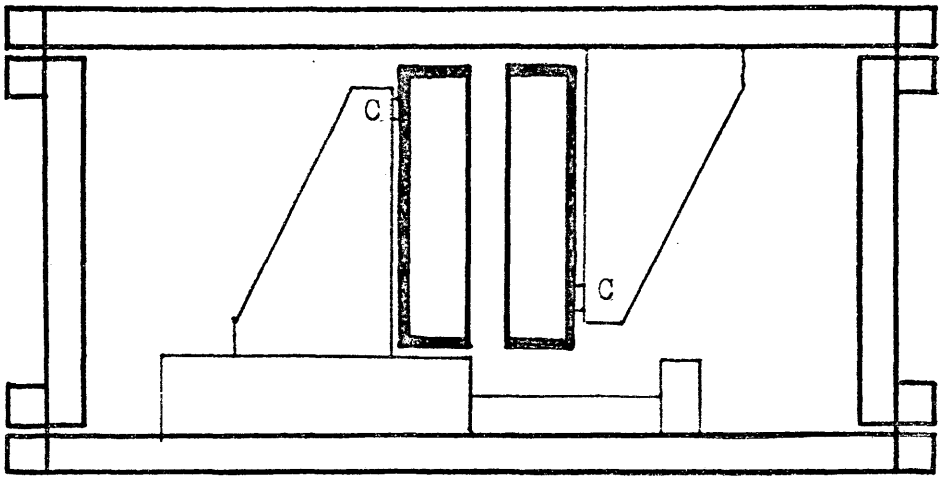

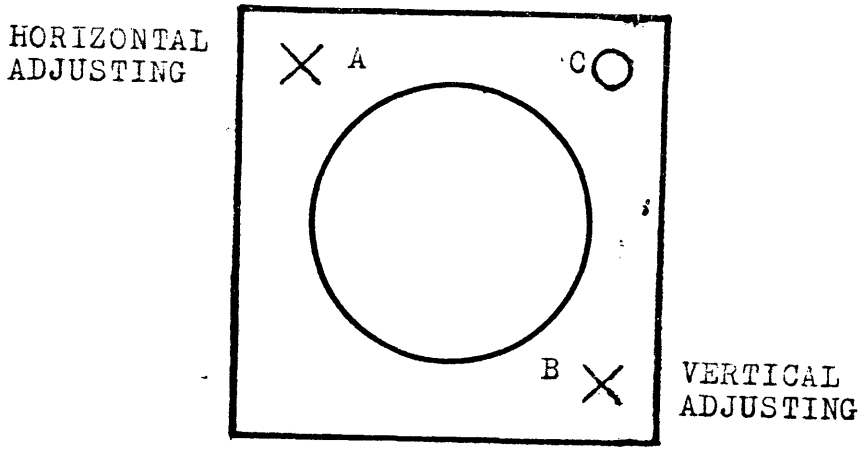

FIG. 14 MOUNTING OF FABRY-PEROT PLATES

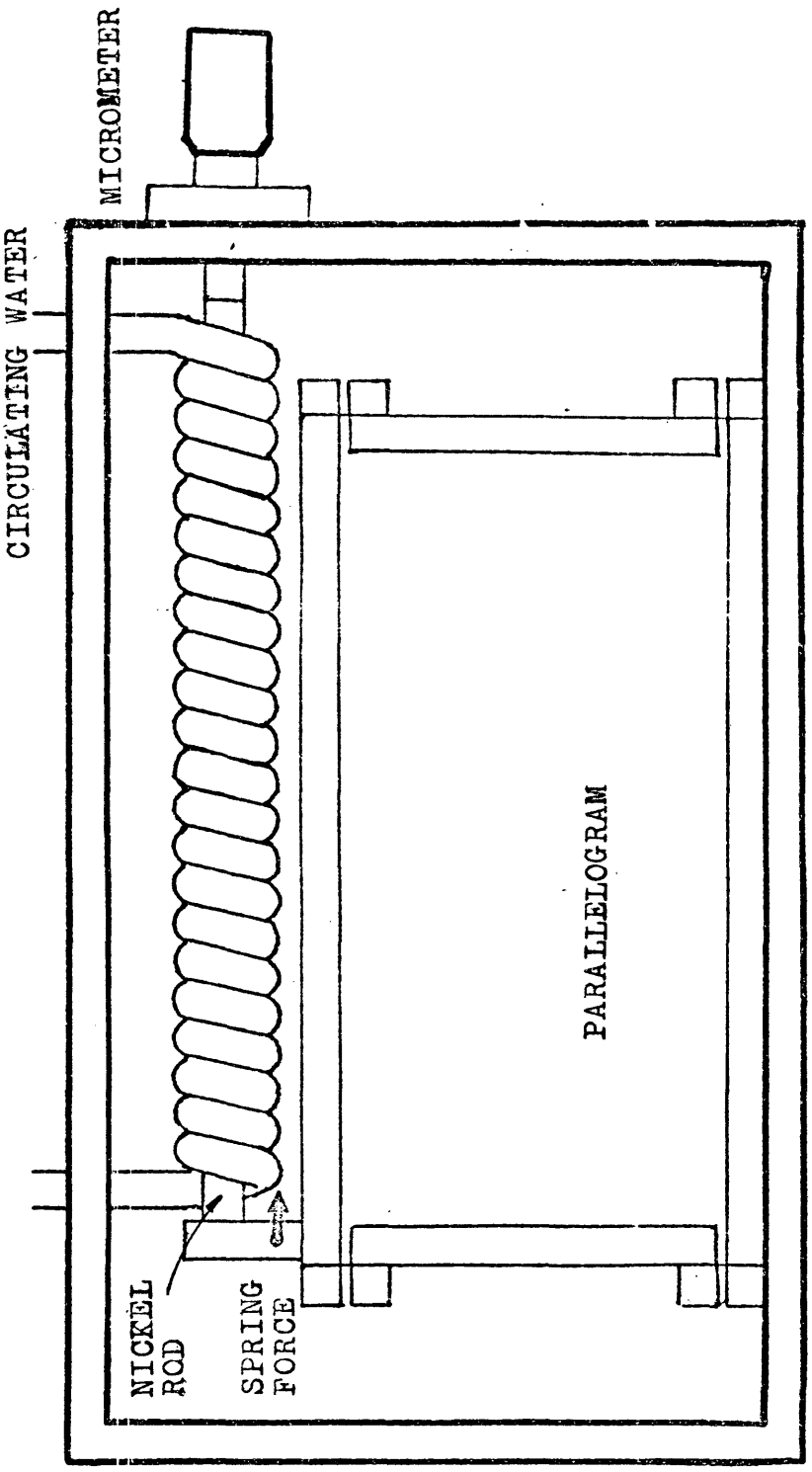

FIG. 15 PRODUCING VARIABLE SPACING

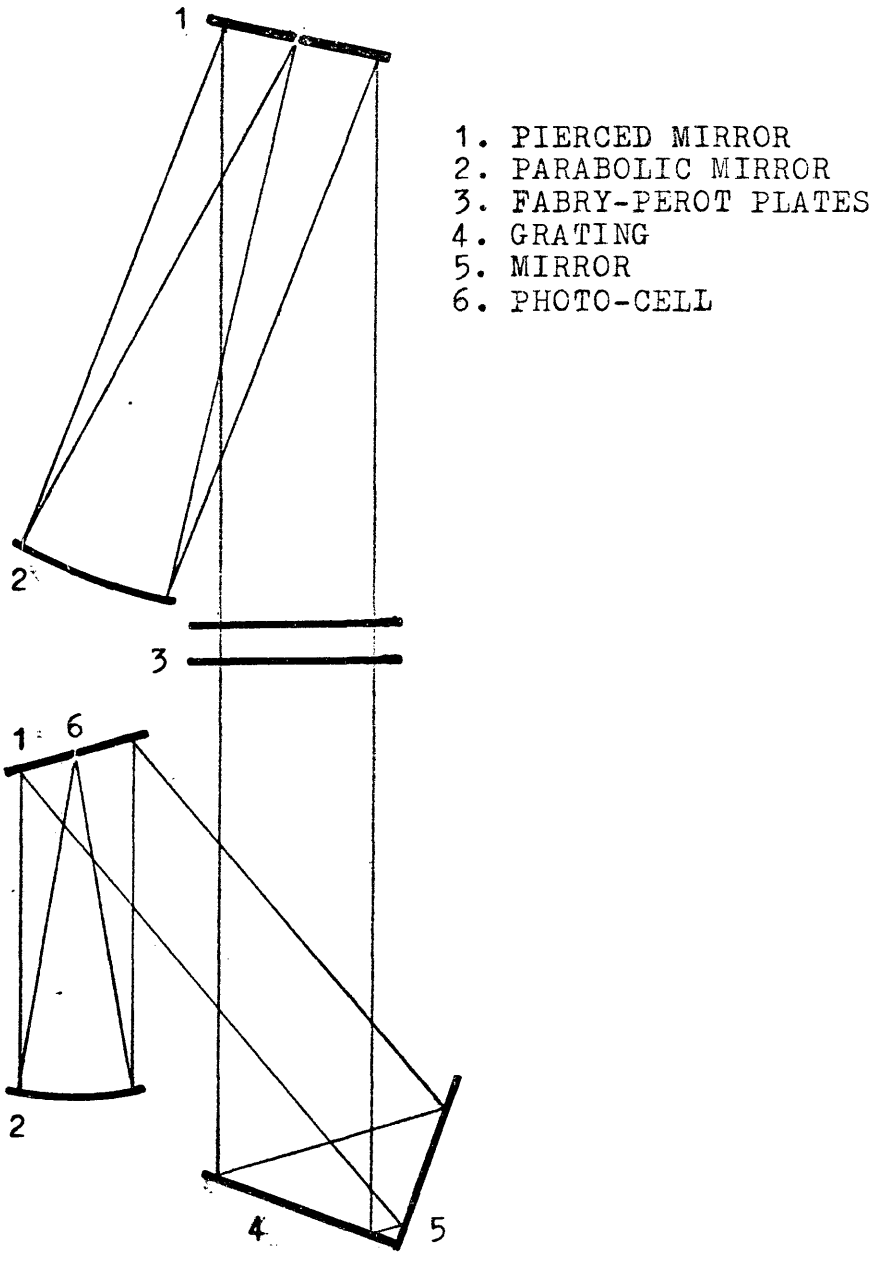

1. PIERCED MIRROR
2. PARABOLIC MIRROR
3. FABRY-PEROT PLATES
4. GRATING
5. MIRROR
6. PHOTO-CELL

Fig. 16 THE OPTICAL SYSTEM

First, by using a lens, the image of the light source is focused on the hole of the first pierced mirror. Because the focus of the parabolic mirror is right on the hole, the outgoing light is a parallel beam and is perpendicular to the interferometer plates when the pierced mirror is properly adjusted. After the light goes through the interferometer and hits the blazed grating, another parabolic mirror focuses the dispersed light on a photo-cell behind the hole in the second pierced mirror. There are adjusting screws on each of the mirrors for the alignment of the light beam.

The system has advantageous design using a Wadsworth constant deviation mounting of the blazed grating. Figure 17, the maximum concentration of light occurs at an angle $2\alpha + \theta$ from the normal of the macroscopic plane of the grating, where α is the blaze angle and θ is the angle between the normal and incident light. The dispersed light is then reflected by the mirror perpendicular to the grating. The angle between incident light and reflected light is always 2α for whatever the θ. The dispersion relation can be written as

$$d (\sin \theta' - \sin \theta) = m \lambda \qquad (39)$$

where d is the groove distance, θ' is the angle of dispersed light and equals $\theta + 2\alpha$ for maximum brightness. Therefore changing θ will change the wavelength of maximum brightness. A gear system with digital counter varies θ. A similar system is used for the mirror with the photo-cell to choose α . From equation 30, we can calculate the θ value for any desired wavelength of maximum

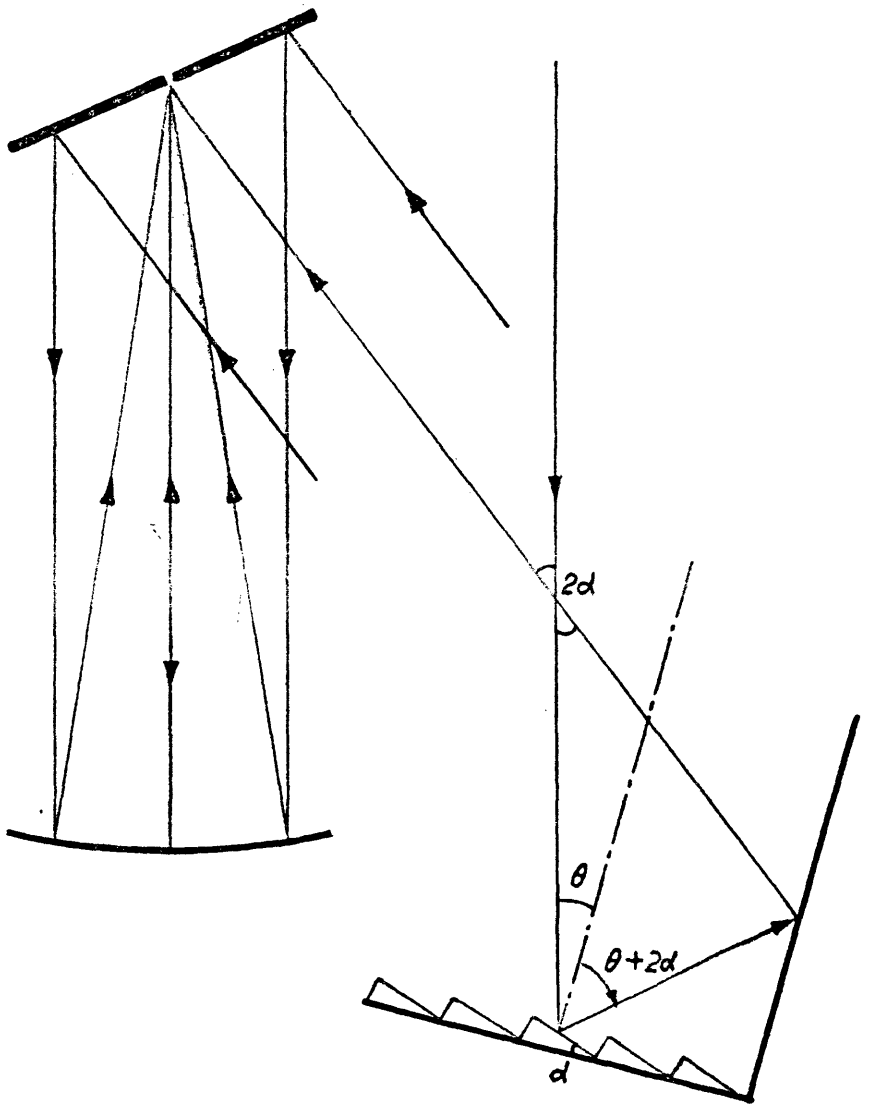

Fig.17 The Grating Mounting

$m\lambda_{max}$ falls on the cell.

A small second photocell is mounted on a small movable rod in front of the second pierced mirror detecting a different wavelength in the neighborhood of $m\lambda_{max}$. Or we can let the He-Ne laser beam shine through the interferometer and be detected by the second cell. Because of the brightness it is advantageous sometimes to use the laser for comparison. The ratio of the digital counter reading to the angle of the grating θ is 800 counts/2.5°. From this, the wavelength falling on the photocell can be calculated. In practice, both the bright Hg source and the He-Ne laser were used to calibrate the counter. The calibration curve is shown in Figure 18 together with a tracing of the Hg spectrum to show how it was obtained.

III-2 THE ELECTRONIC SYSTEM

The system of amplifying and recording the signal from the photocell consists of one self-built amplifier and one commercial Princeton Applied Research (PAR) lock in amplifier. Their outputs feed into a Brown two-pen recorder. Each pen independently records one of the outputs. A block diagram of the whole system is shown in Figure 19. The two amplifiers use the same reference signal from the PAR optical blade chopper.

III-2.1 NEW AMPLIFIER

The new amplifier was built in a modular design to permit easy changing of its components. The arrangement used is shown in a block diagram in Figure 20.

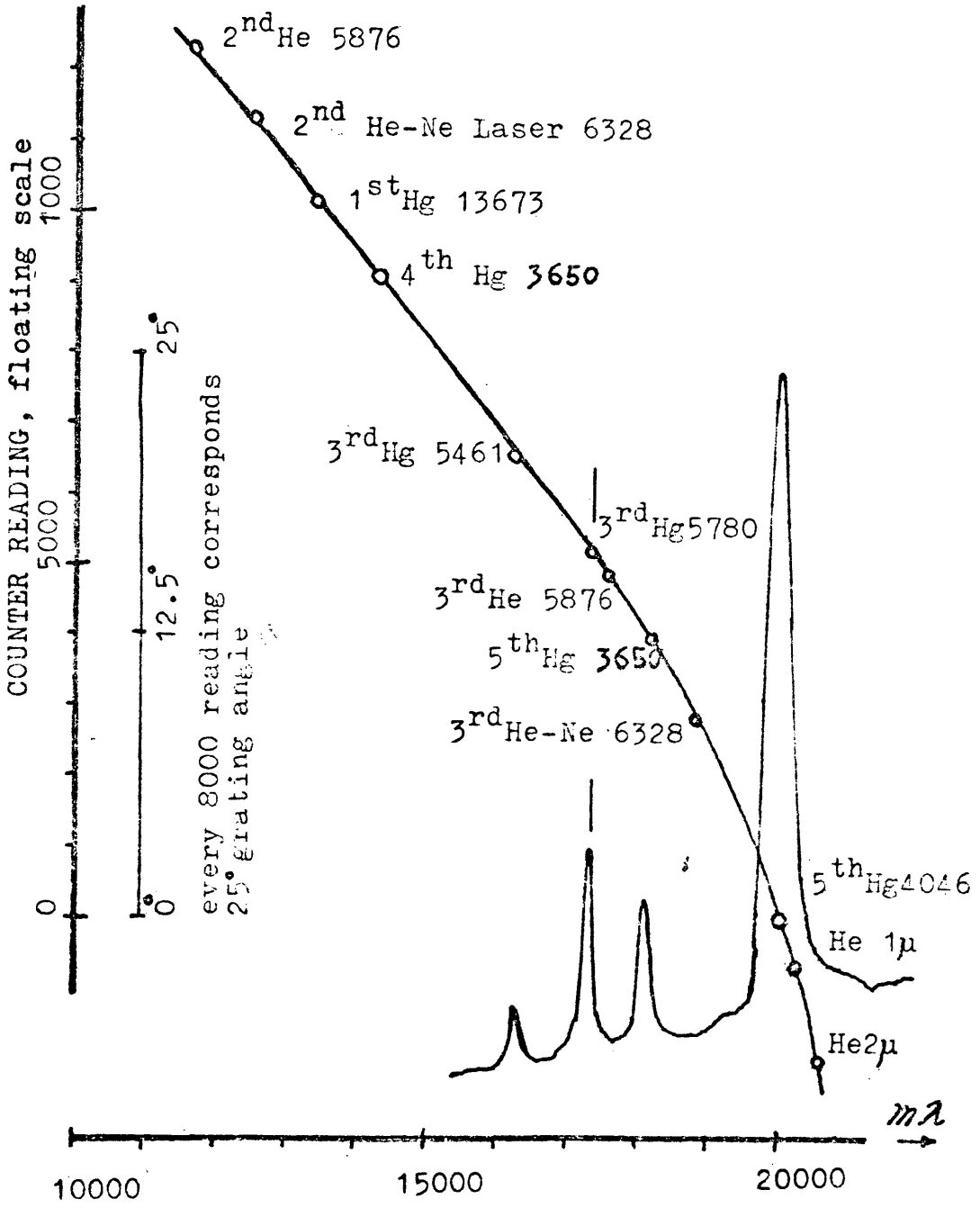

FIG. 18. The Calibration of the Grating Angle Angle Counter Related to $m\lambda$. The Tracing of Hg Spectrum Shows the Determination of λ.

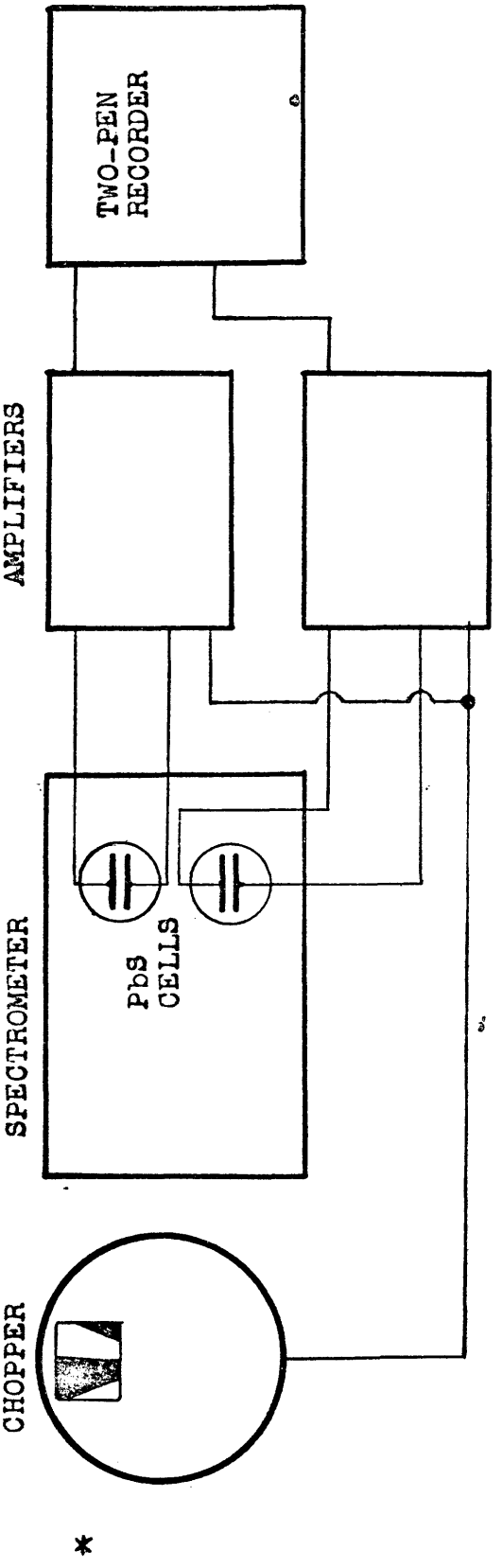

FIG.19 THE ELECTRONIC SYSTEM

The function of the amplifier is to pull the signal V_s out of the noise and offset voltage of the preamplifier V_o. The light beam into the optical system is chopped by a commercial PAR motor driven blade chopper. The PbS photocell produces a pulsed signal from the chopped light. The amplifier demodulates the signal, separating it into two parts, one including V_s plus V_o, the other having only V_o. Subtracting them frees the signal.

At point 1 in Figure 20, the chopped light detected by the photocell generates a voltage signal shown in Figure 21a. That signal and its inherent noise shown at Figure 21B is amplified by a tuned amplifier and appears at point 2 as shown in Figure 21c. At point 3 the reference signal from the chopper is shown in Figure 21d. After shifting its phase appropriately, and adjusting its width, as shown in Figure 21e, it drives a Bristol Synchroverter Switch. This switch then alternately connects the amplifier output to points 5 and 6. When the output goes to point 5, the light path is open, giving a signal V_s plus V_o as in Figure 21f. Then the switch is connected to point 6 while the blade cuts off the light to the photocell, giving V_o only at Figure 21g. Each output has an RC filter, which integrates the output of that particular part of the cycle as shown in the dotted lines. The differential amplifier than amplifies the difference between the two outputs, $(V_s+V_o)-V_o$. Thus if the RC constant is long enough to get a consistent average of V_o, it is then compensated, amplified and sent to the recorder. Because the Brown recorder has full scale of only 1mV, a Helipot is used for the needed attenuation.

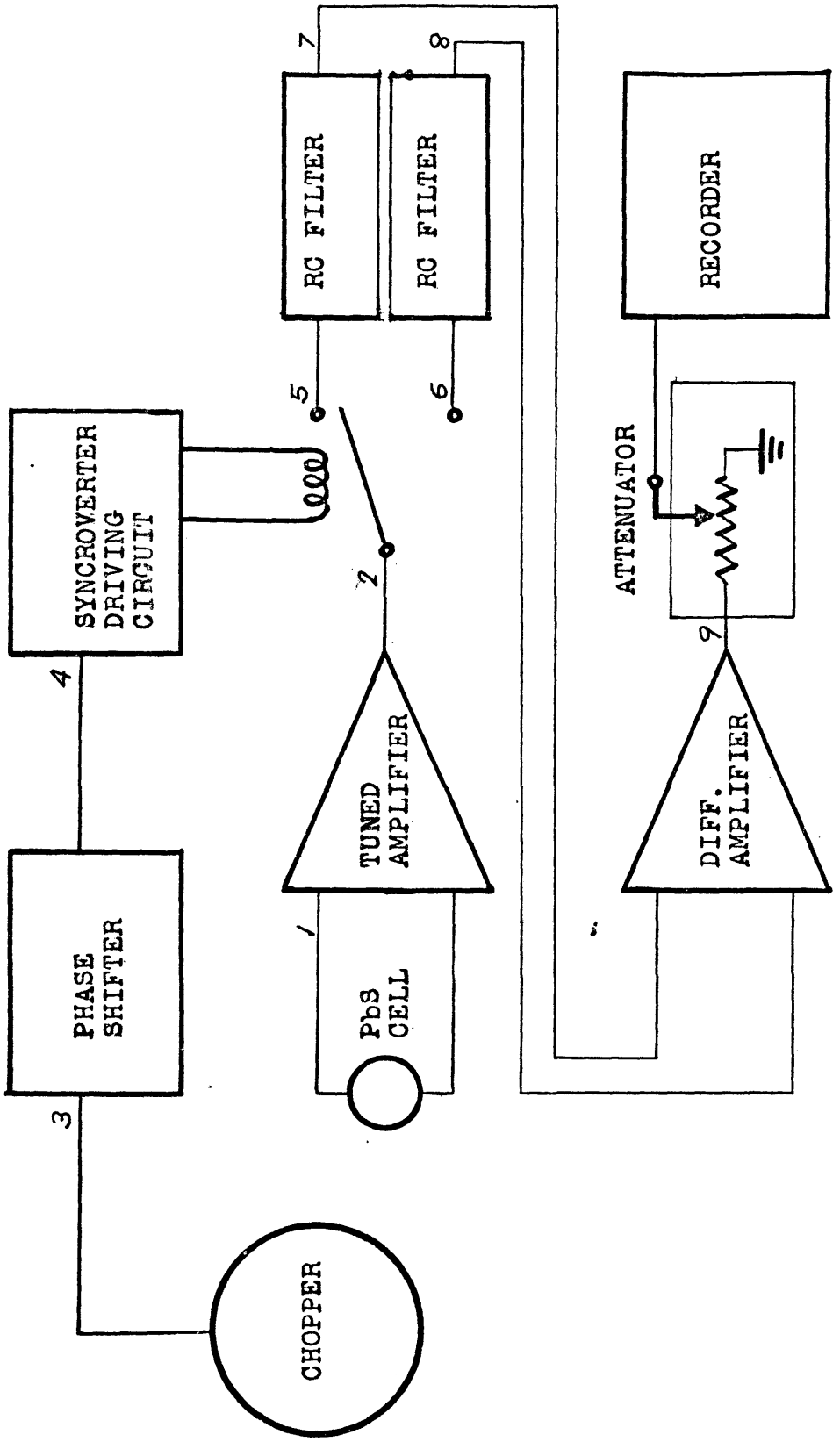

FIG. 20 NEW AMPLIFIER

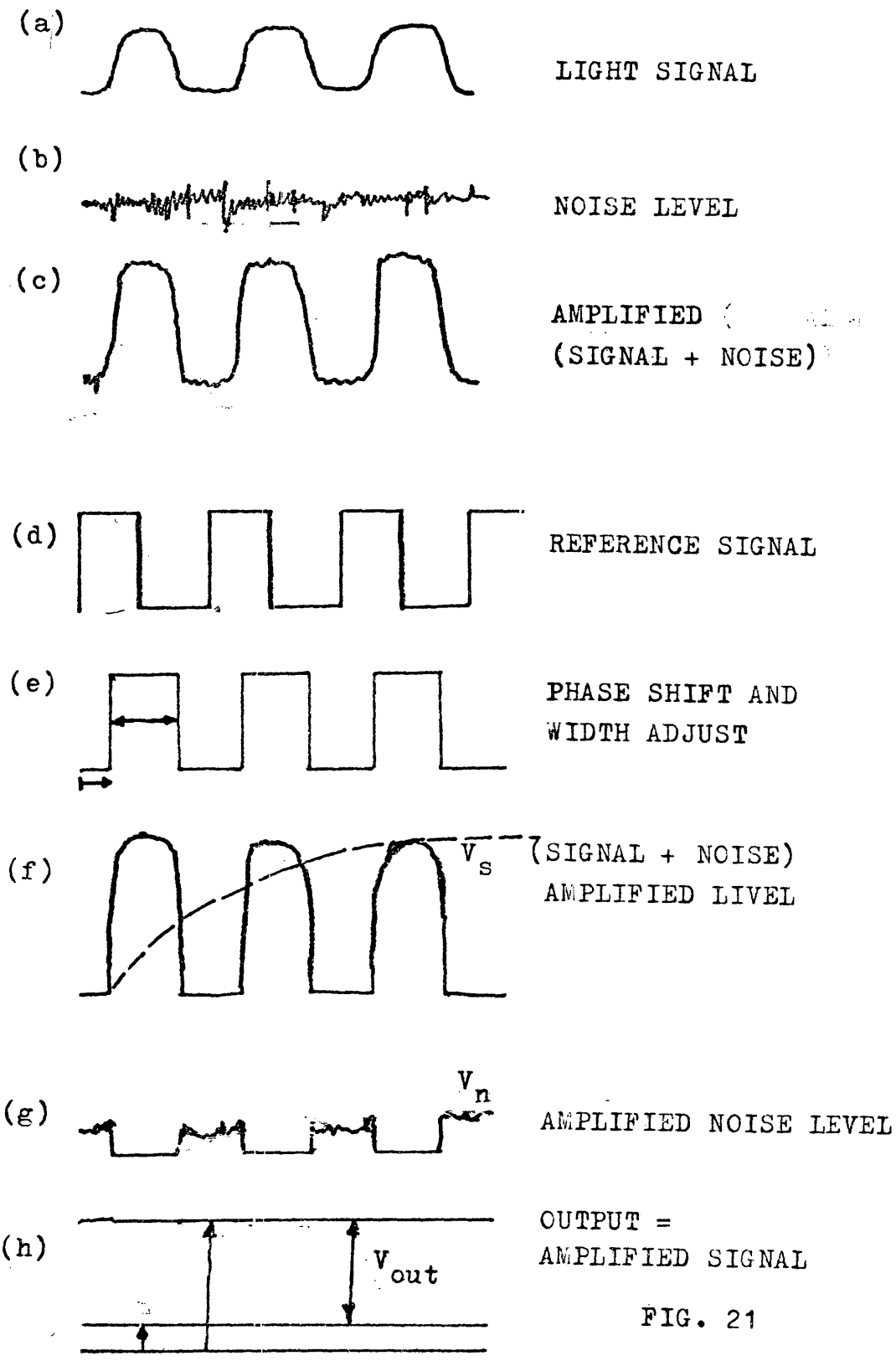
(a)
LIGHT SIGNAL
(b)
NOISE LEVEL
(c)
AMPLIFIED
(SIGNAL + NOISE)
(d)
REFERENCE SIGNAL
(e)
PHASE SHIFT AND
WIDTH ADJUST
(f)
V_s
(SIGNAL + NOISE)
AMPLIFIED LIVEL
V_n
(g)
AMPLIFIED NOISE LEVEL
(h)
V_{out}
OUTPUT =
AMPLIFIED SIGNAL

FIG. 21

III-2.2 PHOTOCELL CIRCUIT

As shown in Figure 22, a 22.5Vbattery serves as voltage source. The resistance of the photocell changes as the intensity of the light changes. The capacitor passes the corresponding voltage variation to the output terminals.

III-2.3 TUNED AMPLIFIER

This simple tuned amplifier uses an integrated circuit operational amplifier with twin-T or bridged-T feedback[58,59] as shown in Figure 23. The tuned amplifier has peak amplification at the notch frequency of the feedback circuit. Figure 24 shows the output characteristics of the completed amplifier of Figure 23. By changing the resistance in the feedback network, the optimum response of the amplifier can be set to the chopping frequency.

The characteristics of a tuned amplifier with twin-T or bridged-T feedback are discussed by Gibson[59], and by Barna[60]. The sharpness of the notch of the feedback circuit is critical to the effectiveness of the system. But, since it is being used mainly to reduce low frequency (1/f) noise and to act as a preamplifier, a sharp notch is not required, and either network is suitable.

III-2.4 DIFFERENTIAL AMPLIFIER

The differential amplifier uses the simple configuration of Figure 25. The characteristic of this configuration is

$$V_{out} = \frac{R_f}{R_i} (V_s - V_o) \qquad (40)$$

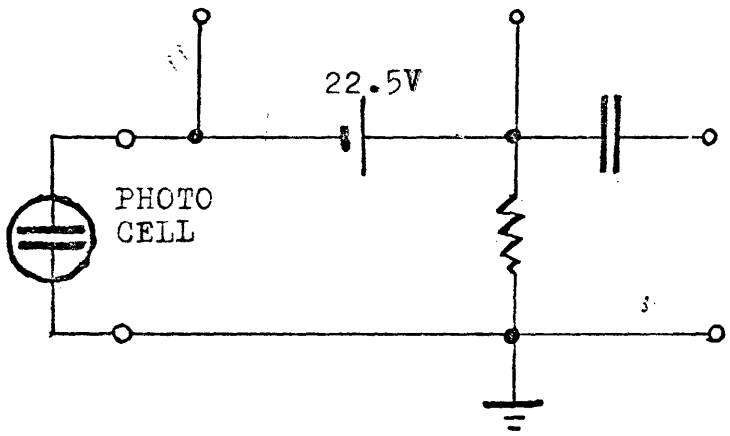

FIG. 22 Photocell Circuit

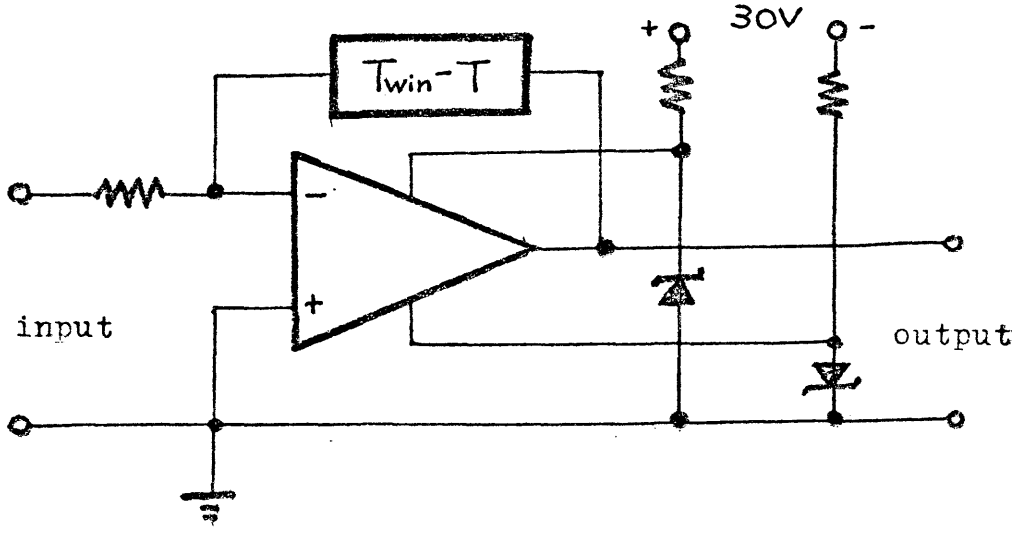

Fig.23 Tuned Amplifier with Twin-T feedback

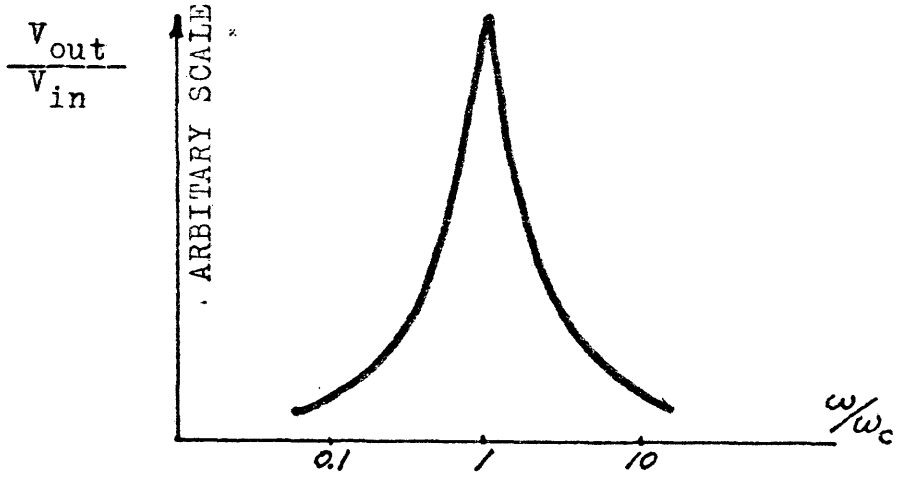

Fig.24 Output Characteristics of an Amplifier with Twin-T Feedback

Gain up to 25 can be obtained with R_i = 1K, R_f = 25k variable.

Another differential amplifier using two IC amplifiers[61] is shown in Figure 26. This one has a characteristic:

$$V_{out} = 2(1 + \frac{R_1}{R_2}) (V_s - V_o) \qquad (41)$$

With the resistor values shown in Figure 26, it has variable gain from 1.04 to a very large value. This amplifier has only one variable resistor, is more convenient to use, and permits easy adjustment of the zero offset.

III-2.5 PHASE SHIFTER

The commercial (PAR) optical blade chopper has a smaller coaxial chopper inside as shown in Figure 27. A small light bulb sends a beam of light through the inner chopper to a photo-transistor, producing a nearly square wave reference signal as shown in Figure 21d. In order for the Syncroverter to demodulate properly, a phase shifter is needed. The phase of the reference wave could be shifted simply by changing the position of the light bulb and the photo-transistor, but this would require repeated opening of the case of the chopper.

Instead, the reference wave is sent to an RC filter, since phase shift is hard to produce directly with a square wave input. The resultant triangular wave is sent to a phase shift network, shown in Figure 28. The output of this network drives a Schmitt trigger circuit to recover a pure square wave for driving the Syncroverter.

The signal to be demodulated is shown in Figure 21c, and redrawn in Figure 29a. If the phase of the chopper is incorrect,

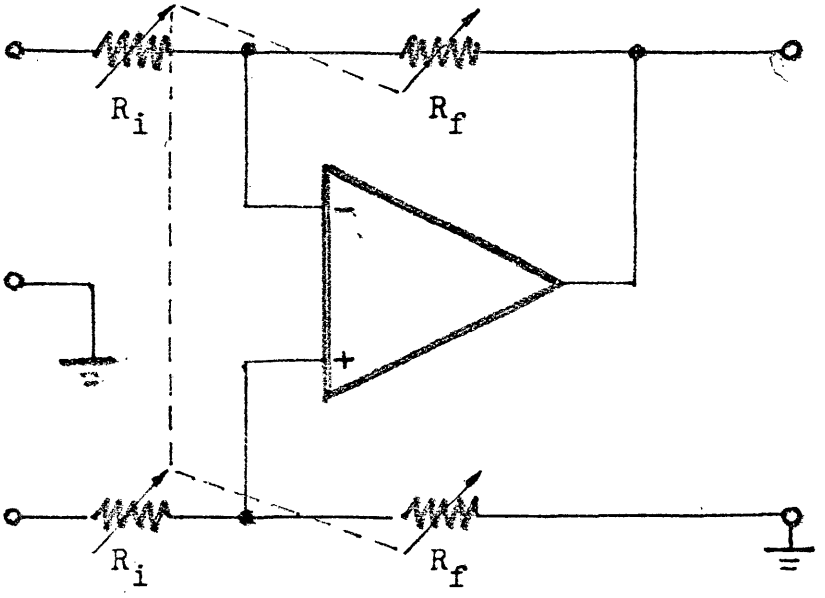

Fig.25 Simple Differential Amplifier

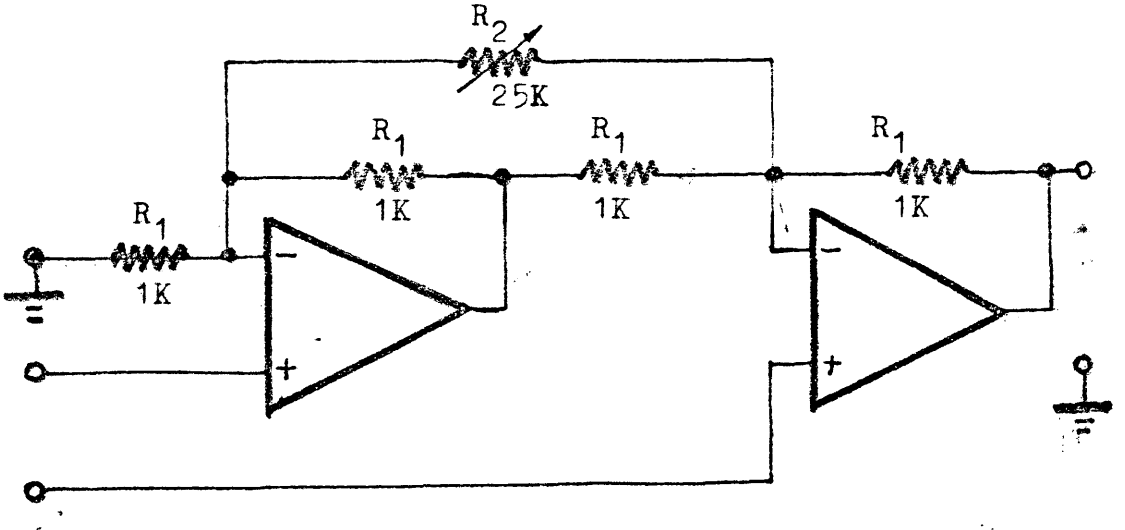

Fig.26 Differential Amplifier Using Two Operational Amplifiers

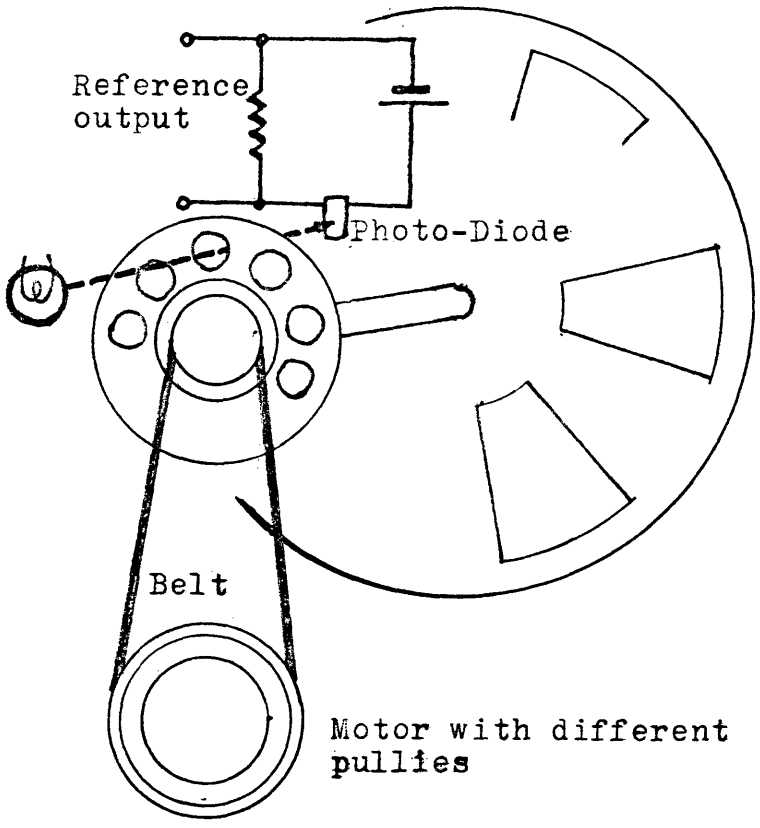

Fig. 27 THE OPTICAL BLADE CHOPPER

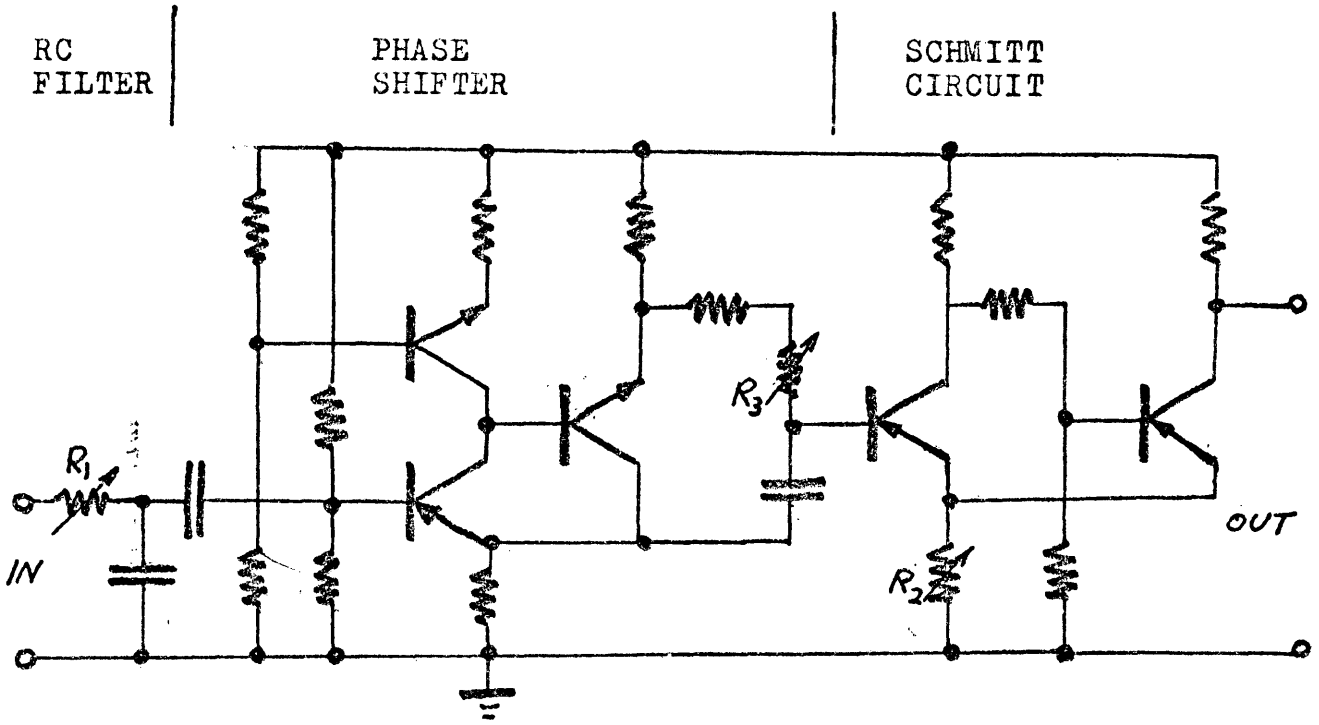

FIG.28 PHASE SHIFTER

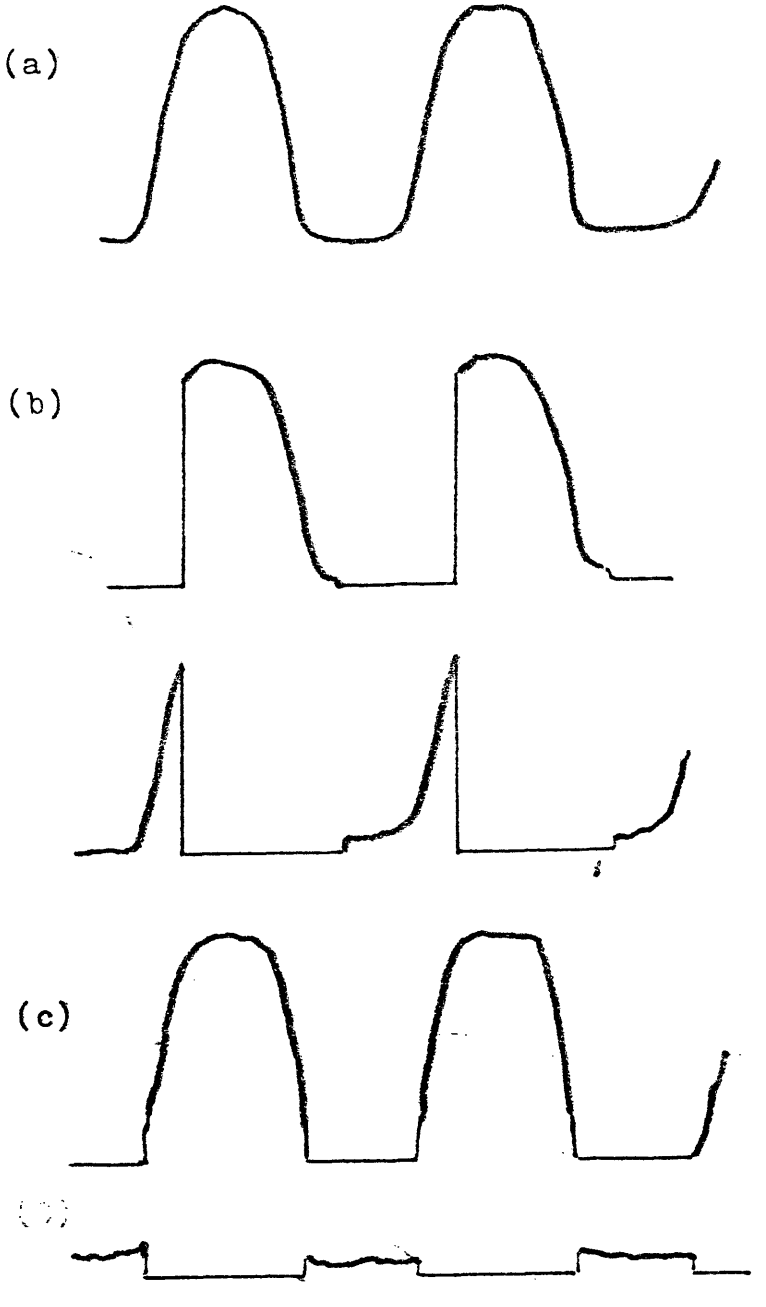

Fig. 29 Output Patterns of the Syncroverter

the output will look like those of Figure 29b. To get optimal operation, not only the phase shift, but the width must be adjusted properly. A phase shift of up to 180° can be provided by changing the values of R_1 and R_2 in Figure 28. The outputs of the synchroverter, points 5 and 6, can be interchanged to get a phase shift up to 360°. Observing these two points on an oscilloscope, adjustments must be made until the pattern matches that of Figure 29c.

III-2.5 THE SYNCROVERTER CIRCUIT

The Syncroverter has low impedance, and needs about 30mA alternating current to drive it. A simple circuit to provide this is shown in Figure 30. When the transistor is on, current flows from A to B. When it is cut off, the shunt current through the coil is in the opposite direction, from B to A.

A second design is shown in Figure 31, using a push-pull circuit which works well for low impedance loads. Figure 31a shows the circuit arrangement, while Figure 32b shows a block diagram of the syncroverter circuit. Both circuits work well, but the push pull uses less power, and gives a sharper square wave to the coil.

III-2.6 RC FILTERS

In the system there are two adjustable RC filters, permitting choice of time constants: .001, .01, .1, 1, 3, and 10 sec.

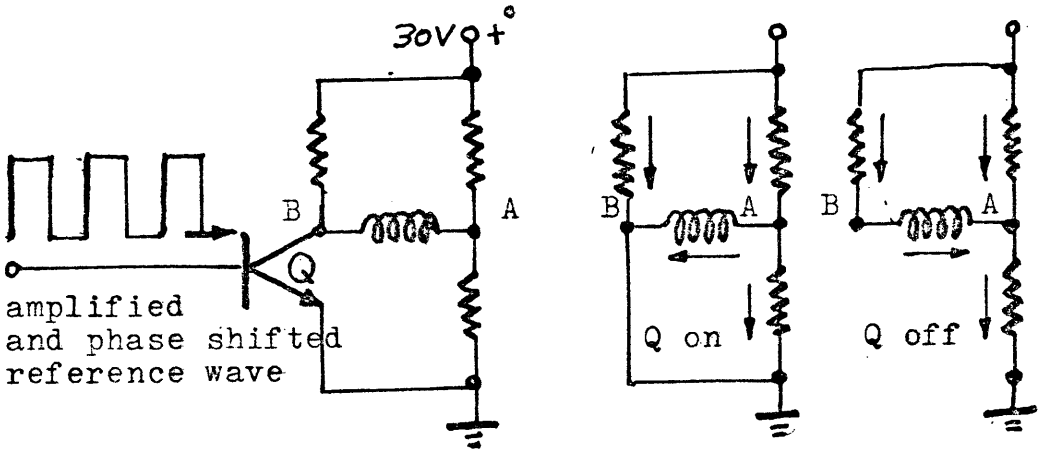

Fig. 30 Simple Syncroverter Circuit

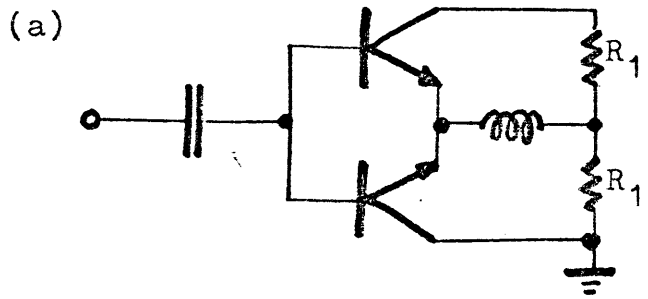

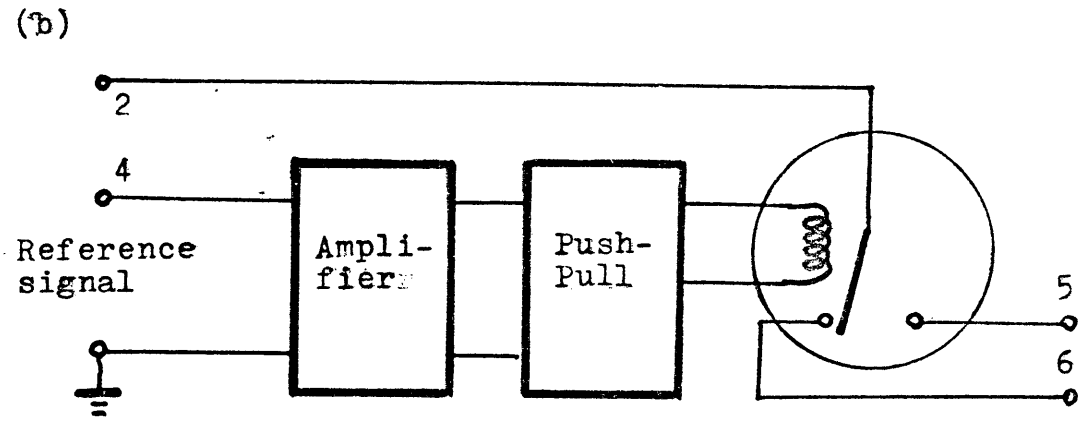

Fig. 31 The Syncroverter Driving Circuit

III-2.7 COMMERCIAL LOCK-IN AMPLIFIER

A commercial (PAR) lock-in amplifier is used for the second photocell, and drives the second pen of the Brown recorder. Its functions are fully described by Diefenderfer[58] and the manual supplied with the amplifier[62].

In comparing the amplifiers, their main functions are the same amplifying two channels independently, with long enough time constant to permit the noise to integrate to a steady value, then cancelling that noise by doing a differential amplification of the two channels. The commercial amplifier is more general, in that it has a much wider frequency range, and can produce its own standard frequency as an output to the experiment. It uses electronic demodulation, where the new circuit uses a mechanical chopper. Keeping the tuned amplifiers to rather wide band operation permits considerable fluctuation of the chopping frequency before going out of the pass band, but again the commercial unit permits easier choice of bandwidth. The greater generality raises the price considerably beyond the single purpose new amplifier.

IV. EXPERIMENTAL METHOD AND RESULTS

IV.1 OPERATION OF THE OPTICAL SYSTEM

IV-1.1 THE HELIUM SOURCE

Commercial Geissler tubes provide a simple light source for general purposes. When the Geissler tube is perpendicular to the observation direction, we get a nice line profile for the He 1μ. However, when capillary is used "end on", the line shape will be widened and the peak intensity reduced as discussed by Kline[57]. When the tube is placed in the magnetic field, the soft glass capillary is heated and quickly breaks. Therefore a Geissler tube must be cooled to release that heat. Unfortunately, the commercial Geissler tubes have a shape that is not to be immersed in liquid nitrogen.

An electrodeless discharge tube made of fused silica has many advantages over a Geissler tube: 1) it runs considerably cooler, reducing the Doppler broadening, 2) it can be heated without cracking in a strong field; 3) the light intensity can be adjusted by changing the output power of the Microtherm which excites the tube; 4) it can be easily cooled by liquid nitrogen because of its compact shape. Regardless of these advantages, the electrodeless discharge tube has one drawback. It is a bulb of diameter of about 1 cm which increases the self-reversal. By reducing the microwave excitation power to the minimum which keeps it going and cooling the tube with liquid nitrogen, the Doppler broadening can be reduced and sharper line obtained.

IV-1.2 DETERMINATION OF INTERFEROMETER SPACING t

A compound interferometer,[63,24] two Fabry-Perot in a series, will form white fringes when one spacing is an integer multiple of the other. With a spacer of known thickness in a small interferometer can be adjusted to a multiple of the known thickness. With four spacers of 3.16mm, 4.12mm, 5.44mm, and 7.12mm, spacings of 1.58, 2.06, 2.72, 3.16, 3.56, 4.12, 5.44, 6.32, 7.12, 8.24, etc. can be found by observing the white light fringes when the small interferometer is put in line with the variable spacing interferometer. By calibrating the micrometer with these observations, it is possible to get any desired spacing within $\pm 10\mu$ when the temperature is kept constant.

IV-1.3 DETERMINATION OF THE ORDER m

First, the method of white light fringes is applied to set a spacing of the interferometer. Then two wavelengths are selected for recording. The two pens on the recorder then show the interference patterns respectively, for example, Figure 32. Circulating warm water expands the nickel rod, Figure 15, and scans through several orders decreasing t. When the power is removed, the smooth contraction permits ever better recording of the spectrum. From the recording, coincidence of two peaks occurs when

$$2t = m_1 \lambda_1 = m_2 \lambda_2 \qquad (42)$$

With t approximately determined by white light fringes, m_1 and m_2 can be estimated since the wavelengths are known. Then m_1' and m_2' in the neighborhood of m_1 and m_2 respectively can be found such

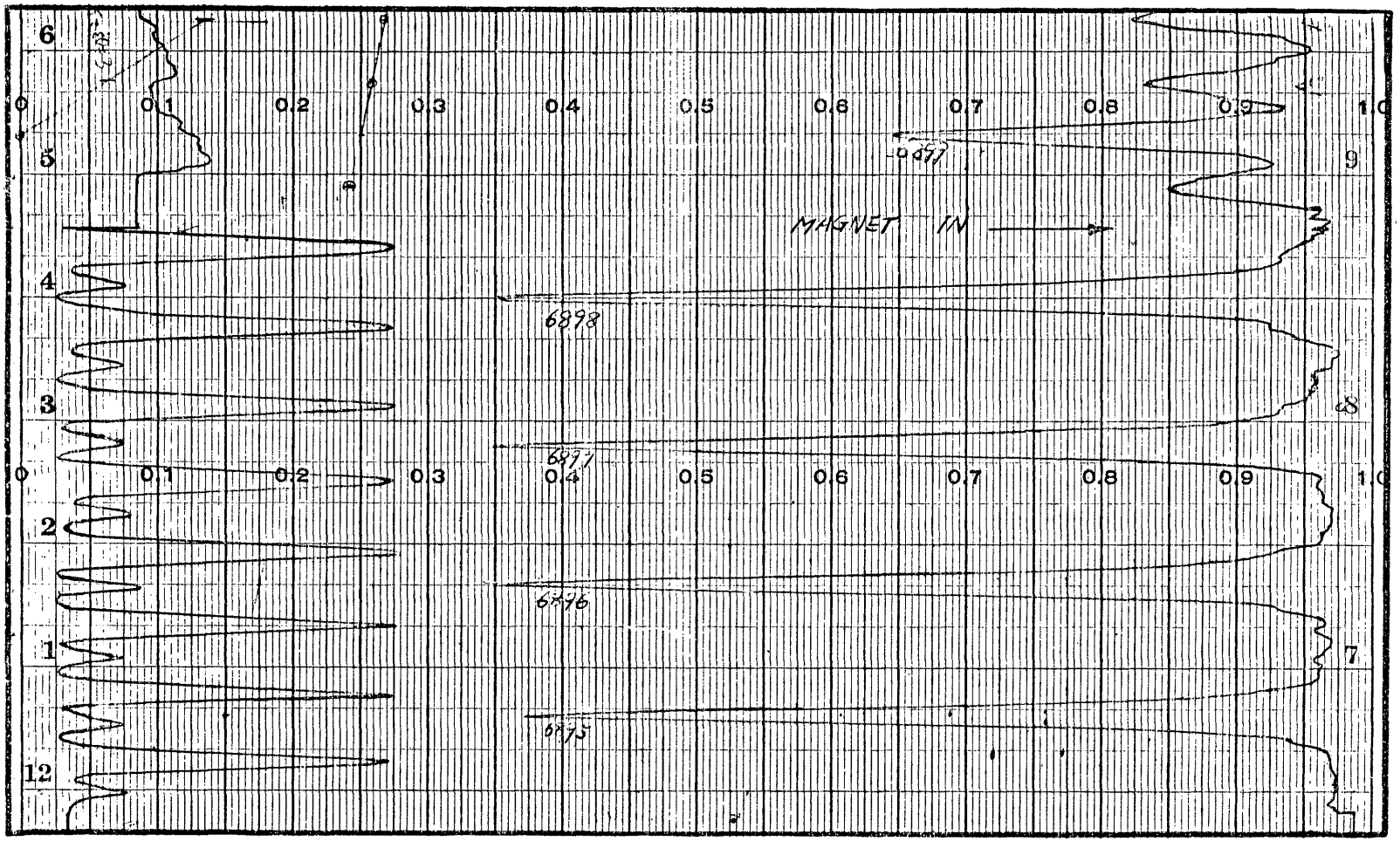

Fig.32 Two-pen recording. Left: He 1μ, right: He 2μ.

that $m_1' \lambda_1 = (m_2' + \epsilon)\lambda_2$ with ϵ very small. Usually an order difference of less than 0.02 can be seen, so ϵ must be smaller than 0.02. After determining m_1' and m_2', the order number is known for each peak. Ditchburn[64] and Candler[25] have the discussion of exact order determination.

IV-2. MEASUREMENT OF ZEEMAN EFFECT OF HELIUM 1μ and 2μ LINES

A permanent magnet of approximately 5200 Gauss gives a Zeeman splitting of $\mu_0 H = 0.243$ cm^{-1}. The wavelength of lines in zero field have to be used to calculate the position of Zeeman components. The published wavelength of the two helium infrared lines are listed in Table 5.

	2μ	$^3P_2-^3S_1$	$^1\mu$ $^3P_1-^3S_1$	$^3P_0-^3S_1$
Ignatieff[31]	20581.31±0.02	10830.32±0.01		10829.11±0.02
Kline[57]	20581.22	10830.47		10829.18
Meggers[65] (intensity)	20581	10830.341 (2500)	10830.250 (1500)	10829.081 (500)
Zaidel[66] (intensity)	20581.30 (2085)	10830.34 (5000)	10830.25 (3000)	10829.09 (1000)

TABLE 5

For the calculations in this section, the wavelengths used are shown in Table 6.

$^1P_1 - {}^1S_0$	2.0581 μ
$^3P_2 - {}^3S_1$ $^3P_1 - {}^3S_1$)	1.08303 μ
$^3P_0 - {}^3S_0$	1.08291 μ

TABLE 6

IV-2.1 MEASUREMENT OF He 2μ ZEEMAN EFFECT

The expected splitting of this line is the normal Lorentz triplet. Under H = 5200 Gauss, the two S components have a separation of 1.029 Å from the p component while the p component stays at the original position. One of the recordings is reproduced in Figure 33 (see also Figure 32). The order was determined by using white light fringes as described in section IV-1.5. Some of the results are listed in Table 7. Measurement 1 to 10 are done at the interferometer spacing 7.12mm, measurement 11 and 12 are done at 5.50mm.

Because of this discrepancy, the magnetic field was remeasured with a Hall probe Gaussmeter having 2% accuracy. This gave a field strength of 4850 Gauss, and an expected Zeeman splitting of 0.96 Å in excellent agreement with the experimental results.

The uncertainty in the results of different measurements mainly results from the inaccuracy in determining the fractional order ϵ. The calculation of $\Delta\lambda$ is $\Delta\lambda = (\frac{m+\epsilon}{m})\lambda - \lambda = \frac{\epsilon}{m}\lambda$ for S component of longer wavelength and is $\Delta\lambda = (\frac{m+\epsilon}{m+1})\lambda - \lambda = (\frac{\epsilon-1}{m+1})\lambda$ for the S component of shorter wavelength. Clearly the relative error in $\Delta\lambda$ is the same as that in ϵ. So,

$$\frac{\delta(\Delta\lambda)}{\Delta\lambda} = \frac{\delta\epsilon}{\epsilon}$$

The determination of ϵ is no better than 0.01 order. Use of a larger spacing could be helpful.

If a small time constant is used in the RC filters of the amplifiers, the recording will be noisy, particularly for weak lines

requiring high gain. Use of a very long time constant will smooth the output, but if the same scan speed is used, will truncate and offset the recorded peaks. Thus, weak lines must be recorded slowly with long time constant to get correct results.

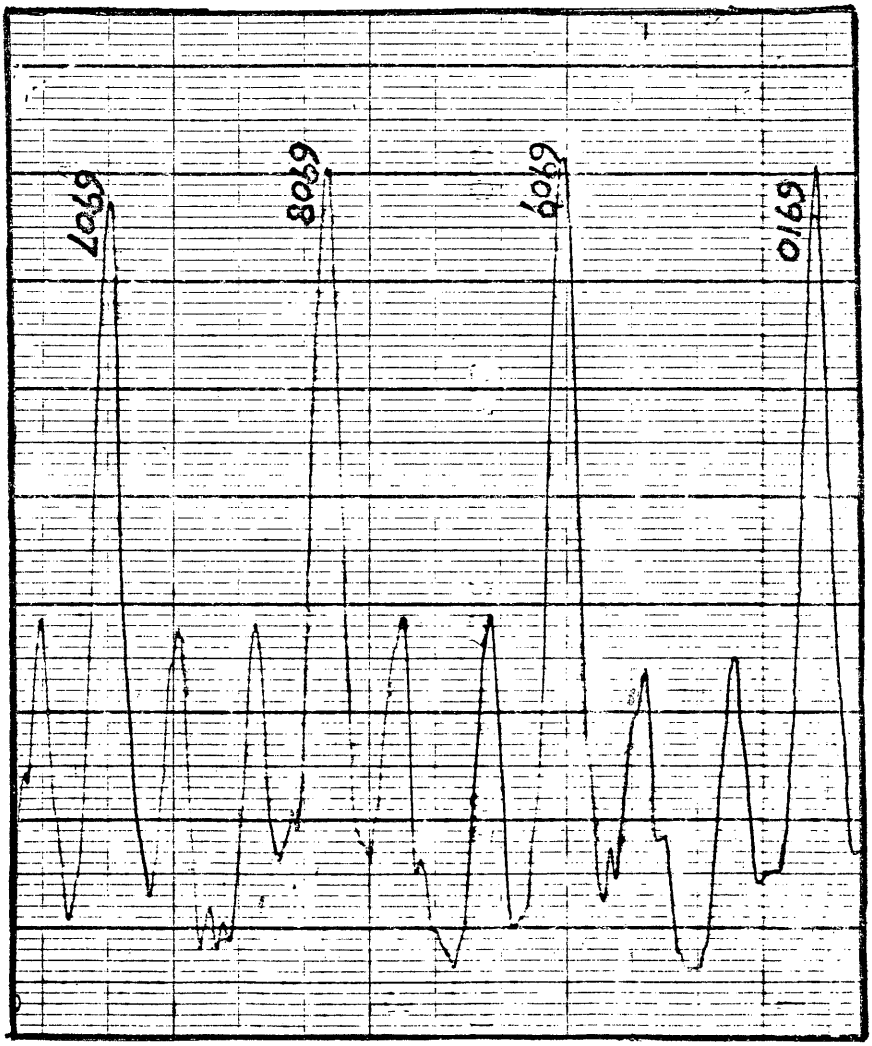

FIG.33 Normal Zeeman Triplet of He 2μ
The number shows the order

	ORDER m	FRACTIONAL ORDER ϵ	$2t$ (μ)	$\lambda(\mu)$	$\Delta\lambda(\mathring{A})$
1	6907	0.680	14216.69621	2.0580046	0.9533
2	6908	0.330	14218.03390	2.0581983	0.9832
3	6908	0.675	14218.74402	2.05800318	0.9681
4	6909	0.325	14220.08178	2.0581968	0.9681
5	6902	0.325	14205.6750	2.05819610	0.9691
6	6902	0.685	14206.4000	2.05800608	0.9392
7	6899	0.325	14199.50078	2.05819695	0.9695
8	6900	0.320	14201.54856	2.05819545	0.9545
9	6899	0.675	14200.22112	2.05800306	0.9694
10	6900	0.680	14202.2895	2.05800456	0.9543
11	5394	0.750	11102.93498	2.05800463	0.9537
12	5395	0.250	11103.96403	2.05819537	0.9537

TABLE 7

IV-3.1 MEASUREMENT OF He 1μ ZEEMAN EFFECT

The expected splitting of these lines in magnetic field was discussed in Section II-3.2. Figure 11 shows the expected pattern. In a Fabry-Perot interferometer, the two stronger lines, $^3P_2 - {}^3S_1$ $^3P_1 - {}^3S_1$ are too close to be resolved and the recording shows a doublet instead of the expected triplet. The interference pattern in a magnetic field is an overlapping of different components, which may even be in different orders. Therefore, the recorded pattern is not that of Figure 11. Because there are so many components, it is impossible to distinguish them from the recorded pattern. Therefore the expected interference patterns of order m are calculated for different components and then overlapped to obtain the over-all pattern at a particular interferometer spacing.

Figure 34 shows the expected pattern, 34(c), compared with the tracing of the recording, 34(a) at the spacing 7.12mm. The two peaks are the same transitions and of same wavelengths (transition 11 and 14). The positions between the two peaks for different wavelengths are calculated and plotted with the line height representing their respective intensity. A stack of 10 microscopic cover glasses at a suitable angle serves as the polarizer. The broken curves and lines in Figure 35 show the s component. Figure 35 is a reproduction of a scan at spacing 7.12mm. The magnet was put in and the gain of the detective system was increased very quickly so the transition of the patterns can be seen. The polarizer was put in and taken out with extra care so the positions of p components and s components were not disturbed.

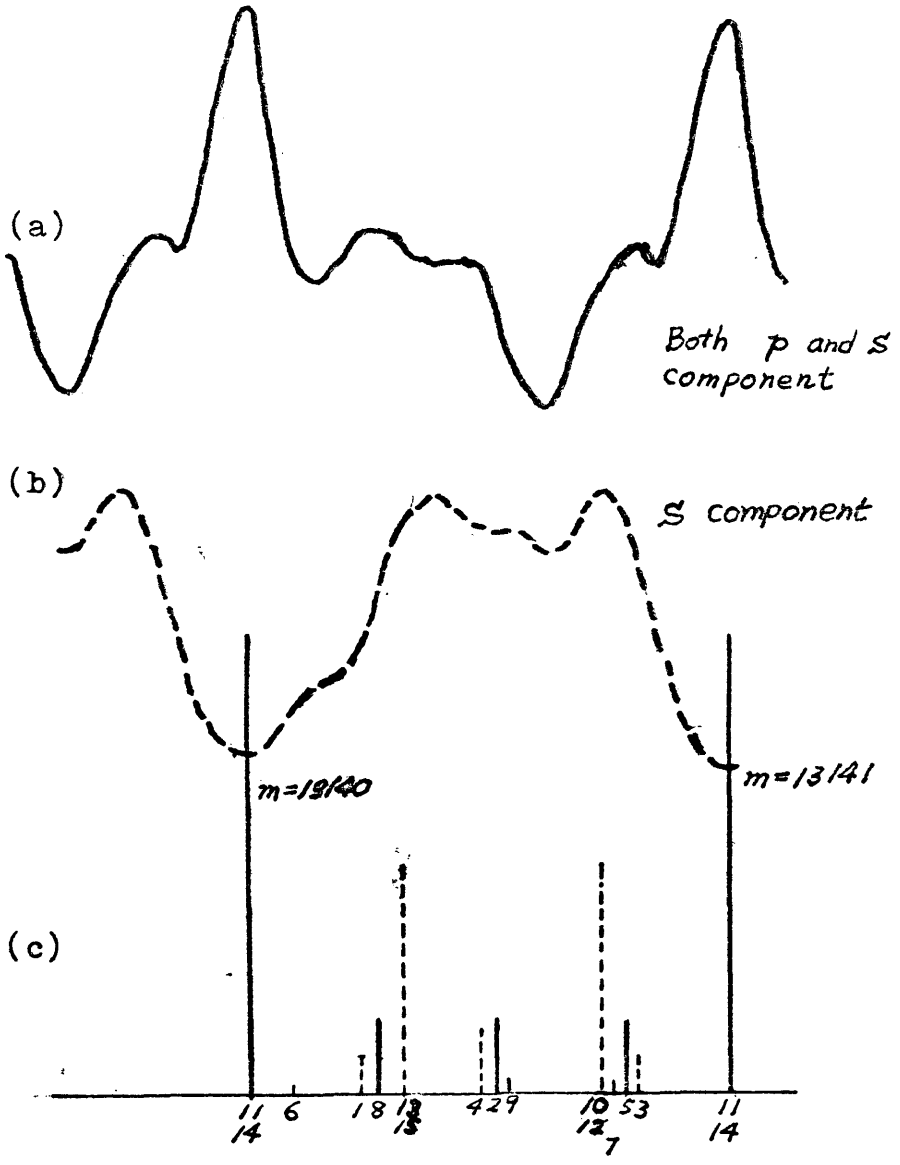

FIG.34 (a) The scanning at spacing 7.12mm.
(b) The observed pattern with polarizer.
(c) Calculated Pattern.

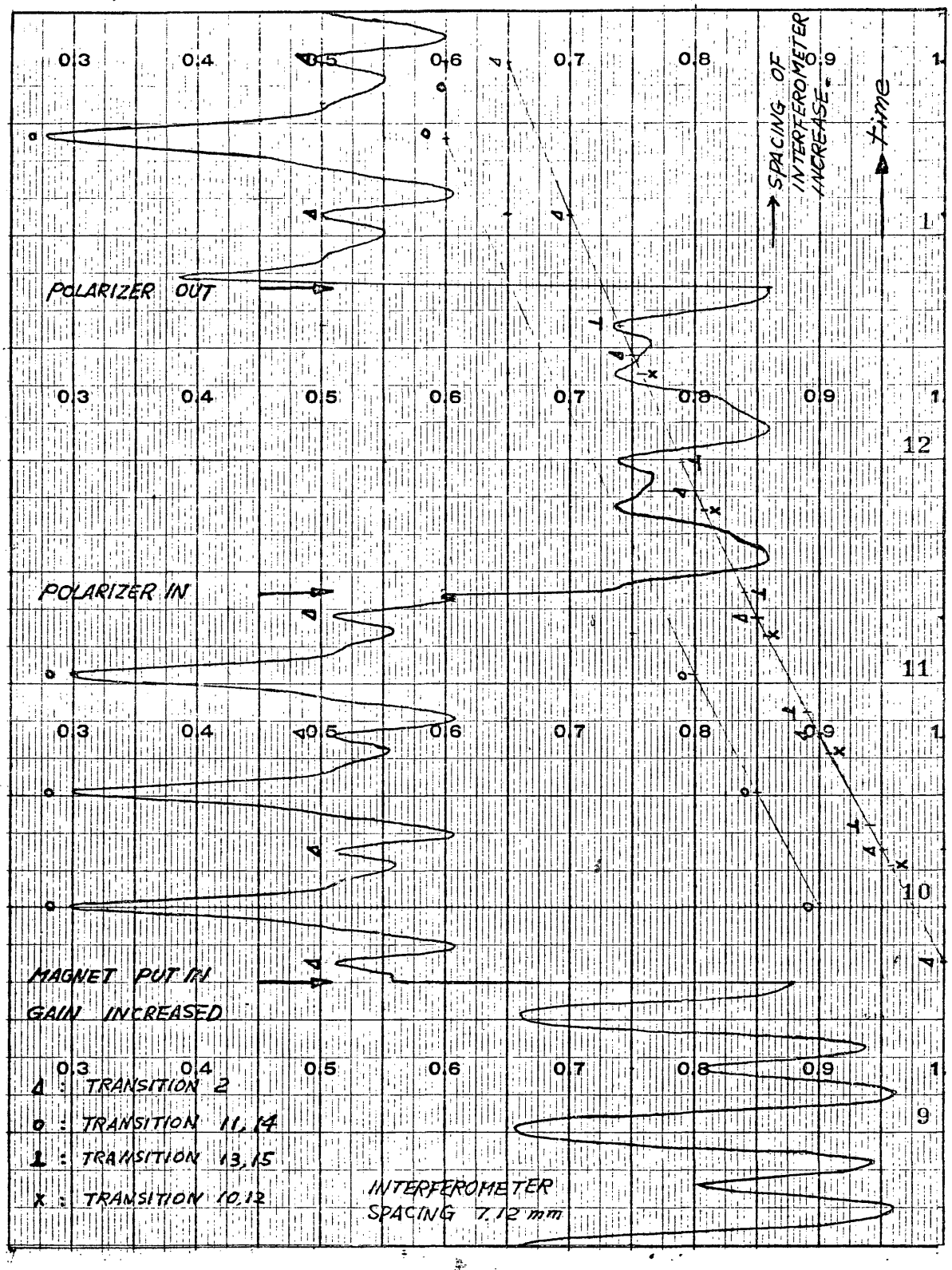

Fig.35 An scan showing Zeeman patterns

From Figure 34, the theoretical prediction fits the experimental result fairly well. Figure 36 shows the repeating patterns of the Zeeman pattern and its s components. As the repeated pattern is continued, it gradually shifts within the basic pattern.

In order to see if the predicted pattern fits at other spacings the recording at 6.75mm is compared to the expected positions and intensities as shown in Figure 37. The expected pattern fits well, but at the positions of transition 1, 2, 3, the relative intensities are higher than that are expected. In Figure 38, also 37a, the smaller peaks marked with x occurs at the position of transition 2. In Figure 39, also 37b, which shows the x component, the peaks marked with Δ are at the position 1. These transitions, numbers 1, 2, 3, come from j=0 the weakest line in the triplet. (According to the sum rule, equation (18), the intensity ratio for the lines in this triplet is 5:3:1 for j=2, j=1, j=0 respectively.) How can they appear to be the strong lines?

The pattern of no field with no splitting is shown at the lower part of Figure 35, and the very left in Figure 39. The pattern of 1 under no field consists of 2 components the stronger component at 10830.3A ($^3P_{1,2} - {}^3S_1$ two lines together) and weaker one at 10829.1A ($^3P_0 - {}^3_1S_1$). The intensity ratio of these two components should be 8:1 as determined by sum rule. However in the recordings, the ratio is only about 1.8:1 (=8:4.5). This is due to the fact that the strong component has equally strong self-absorption, while the weak component in emission is little affected by self-absorption. To take this into consideration, in the patterns of the remaining figures, the predicted relative

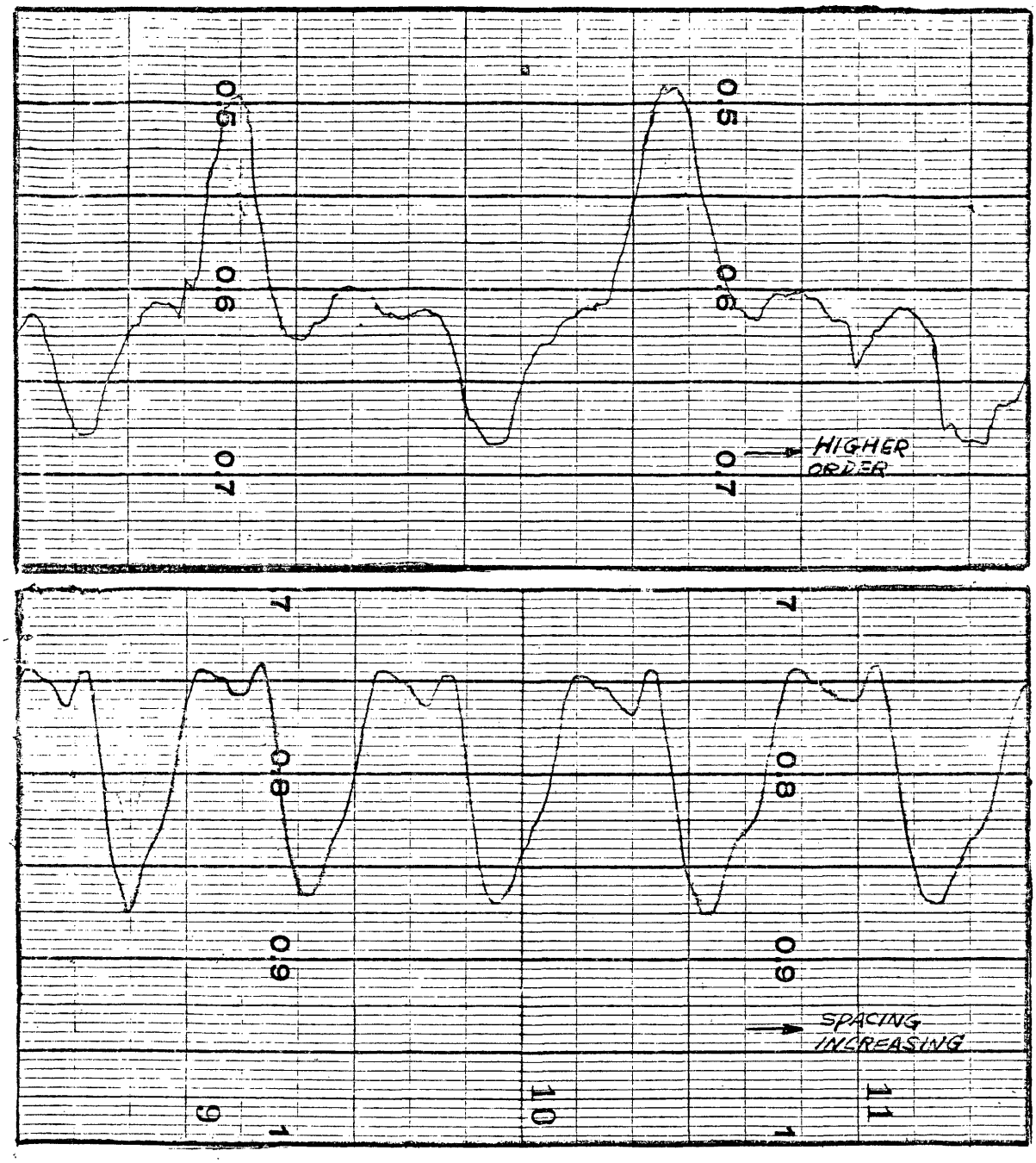

Fig.36 Examples of curve (a) and (b) in fig. 34.

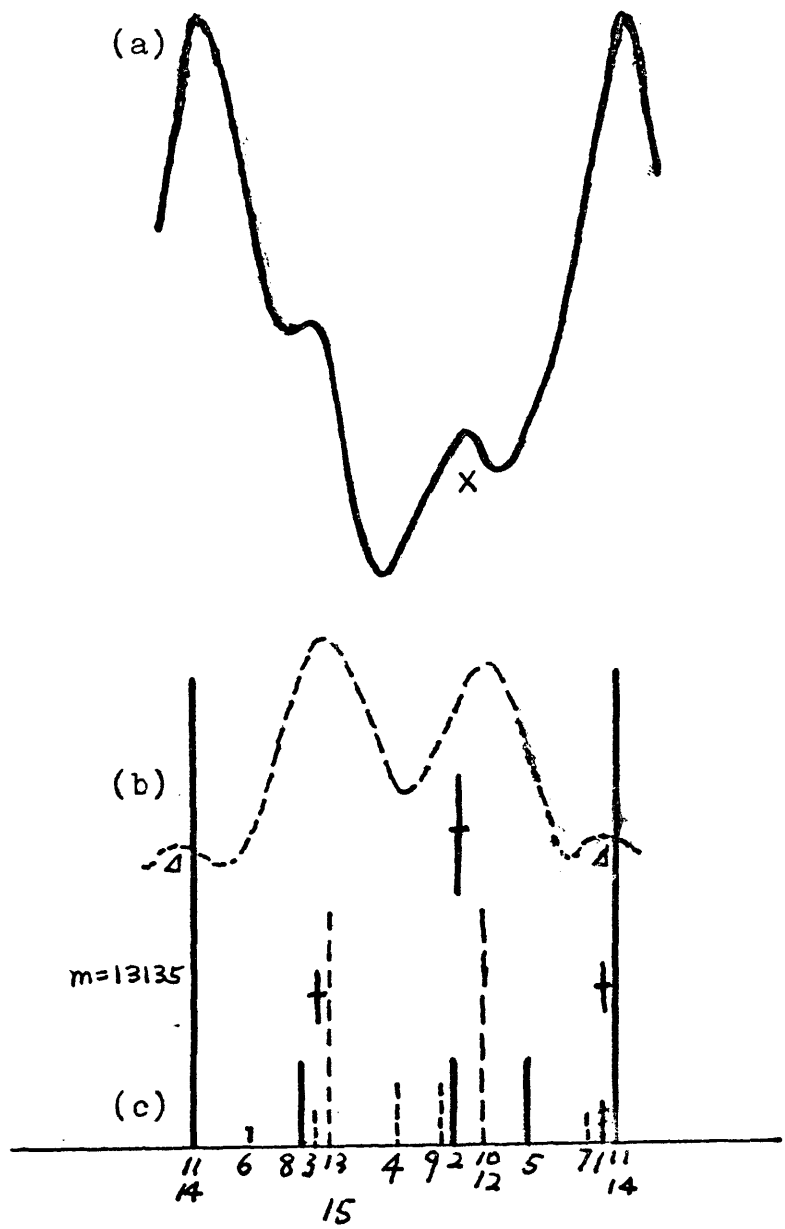

Fig.37 The scanning at spacing 6.75 mm

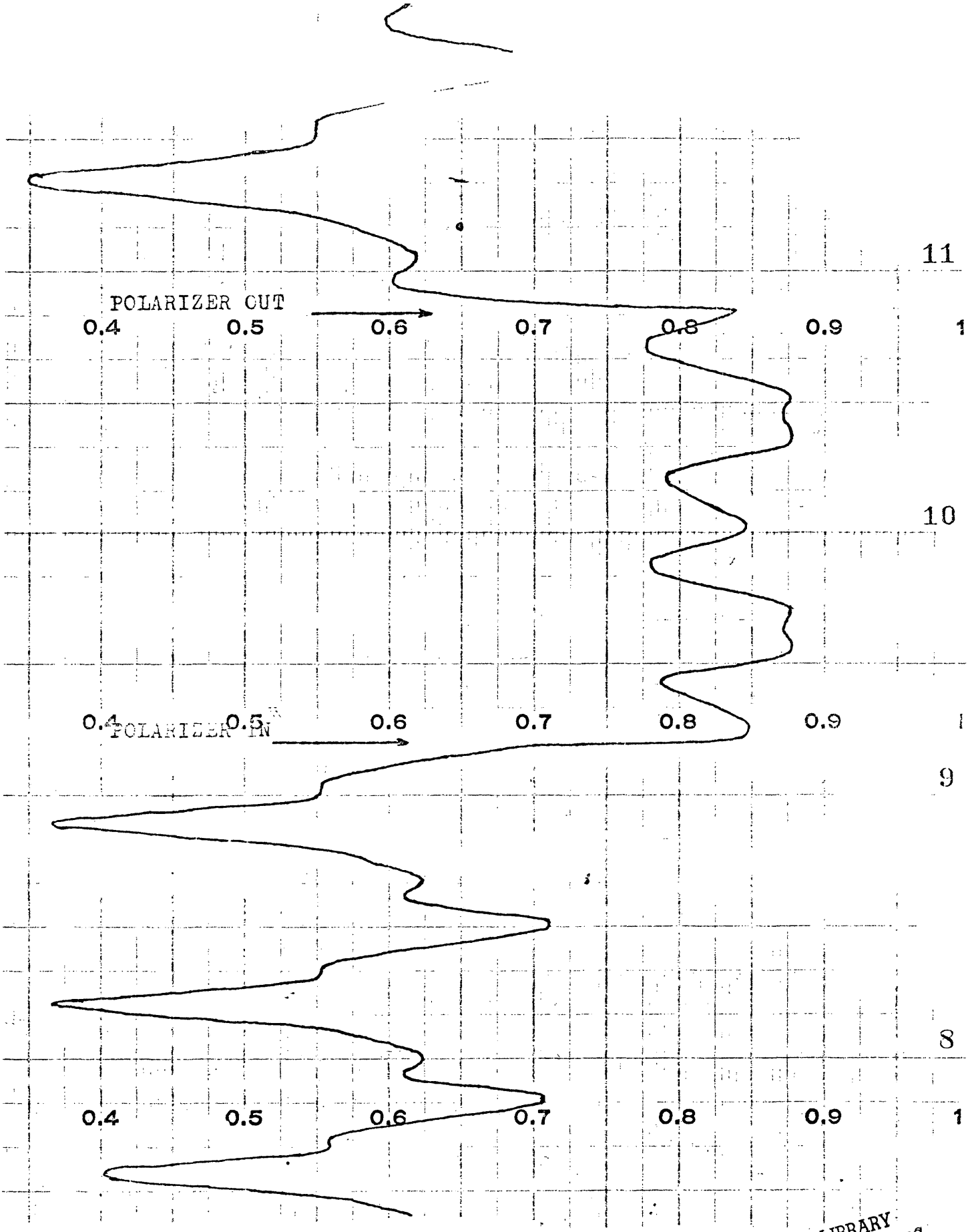

FIG.38 THE SCANNING AT 6.75 mm

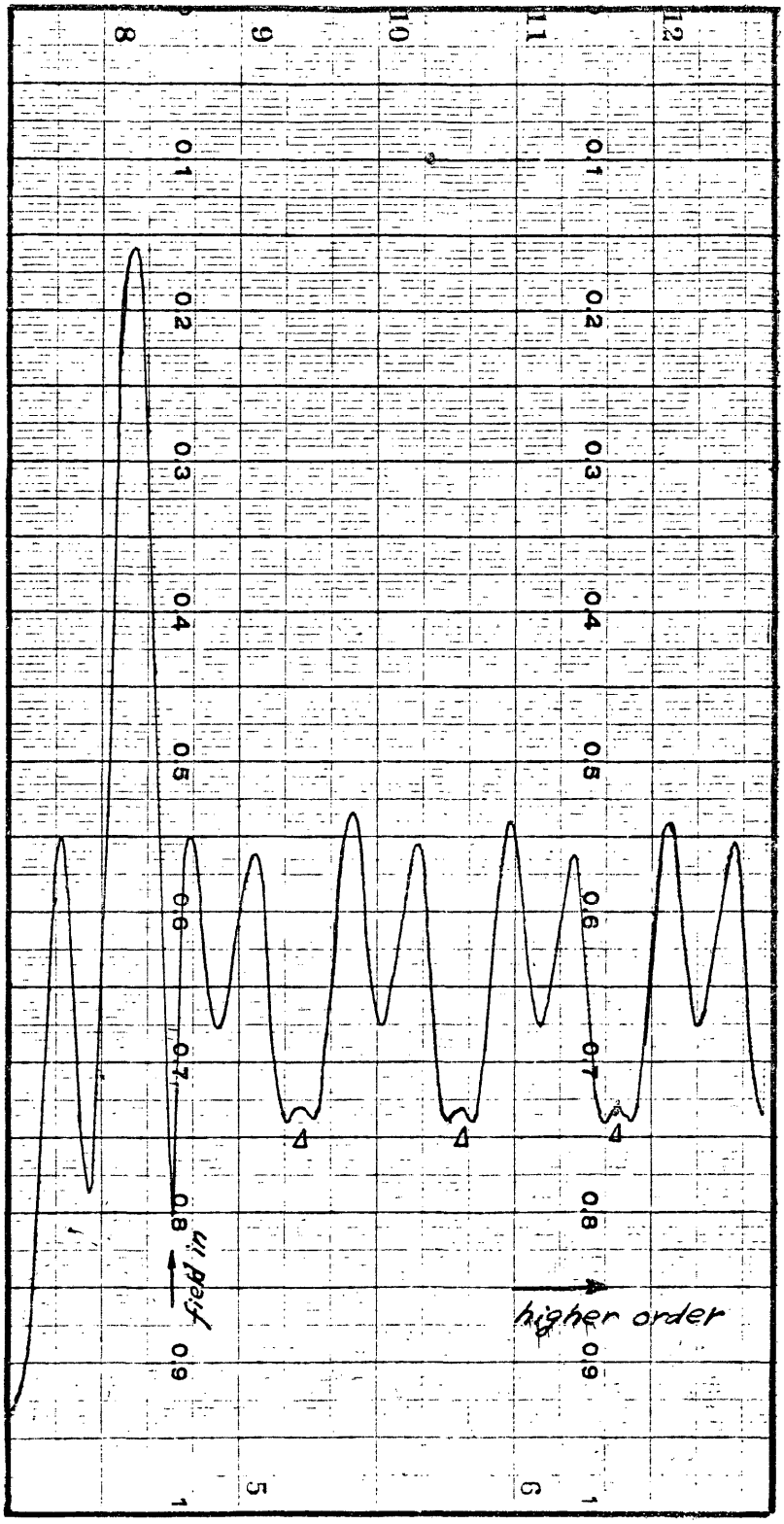

Fig.30 The s component of Paschen-Back pattern scanning at 6.75 mm.

intensity of the $^3P_0$ components has been multiplied by a factor 4.5.

After adjusting the relative intensities for transition 1, 2, 3, the expected pattern fits the experimental result much better. To make sure of this, the results of other measurements done with a different spacing are investigated. Figure 40 is the pattern at spacing of 5.50mm with measured pattern for p and s components together and s component along shown in Figure 41 and 42 respectively. It is obvious without adjusting the intensities, the p component of transition 2 will not fit the strong peak marked with x, Figure 40 and 41, but that the fit is satisfactory after the adjustment.

As a final comparison of the expected pattern and the theoretical prediction, some recordings were made at interferometer spacing of 8.24mm; 9.25mm and 9.50mm, Figure 43. From these, the shift in the interference pattern as the spacing changes can be seen. Among these results, the more interesting pattern, Figure 43a which is the scanning of 8.24mm was studied. Figure 44 shows the result compared with the calculated pattern. The result is found satisfactory.

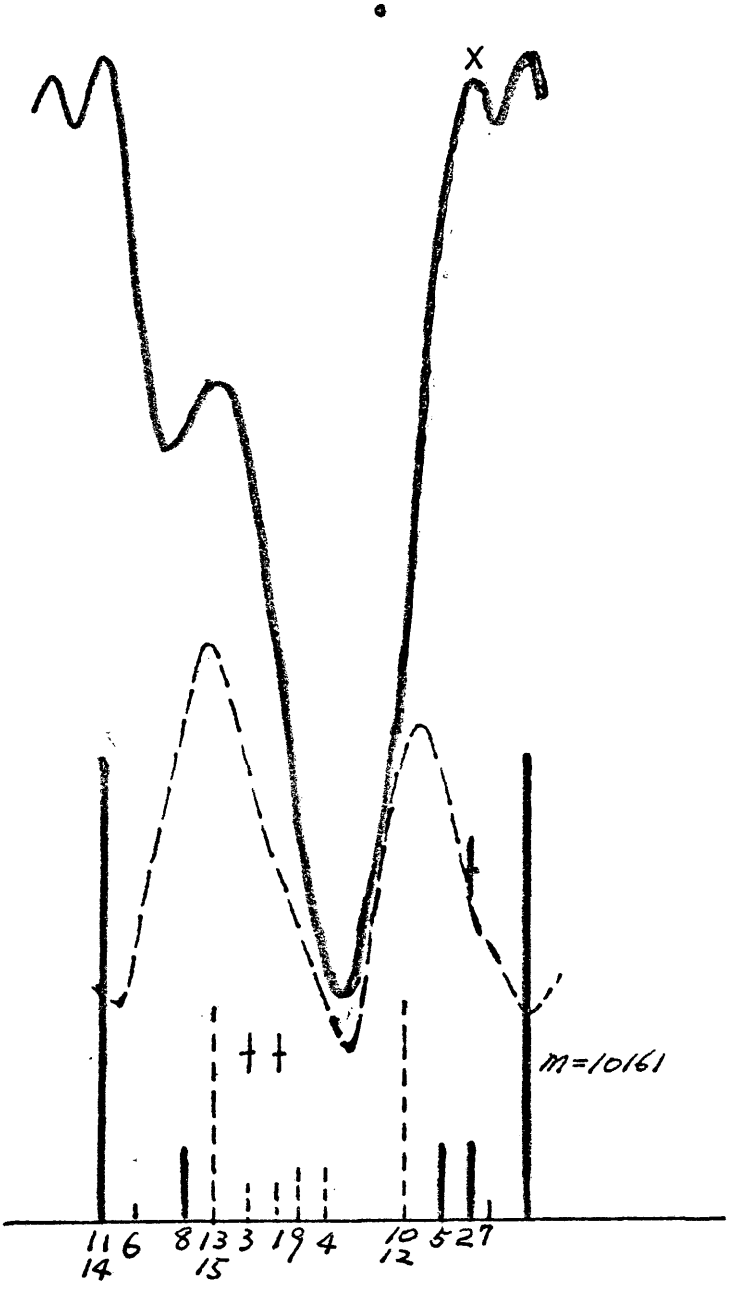

Fig. 40 The scanning at 5.50 mm

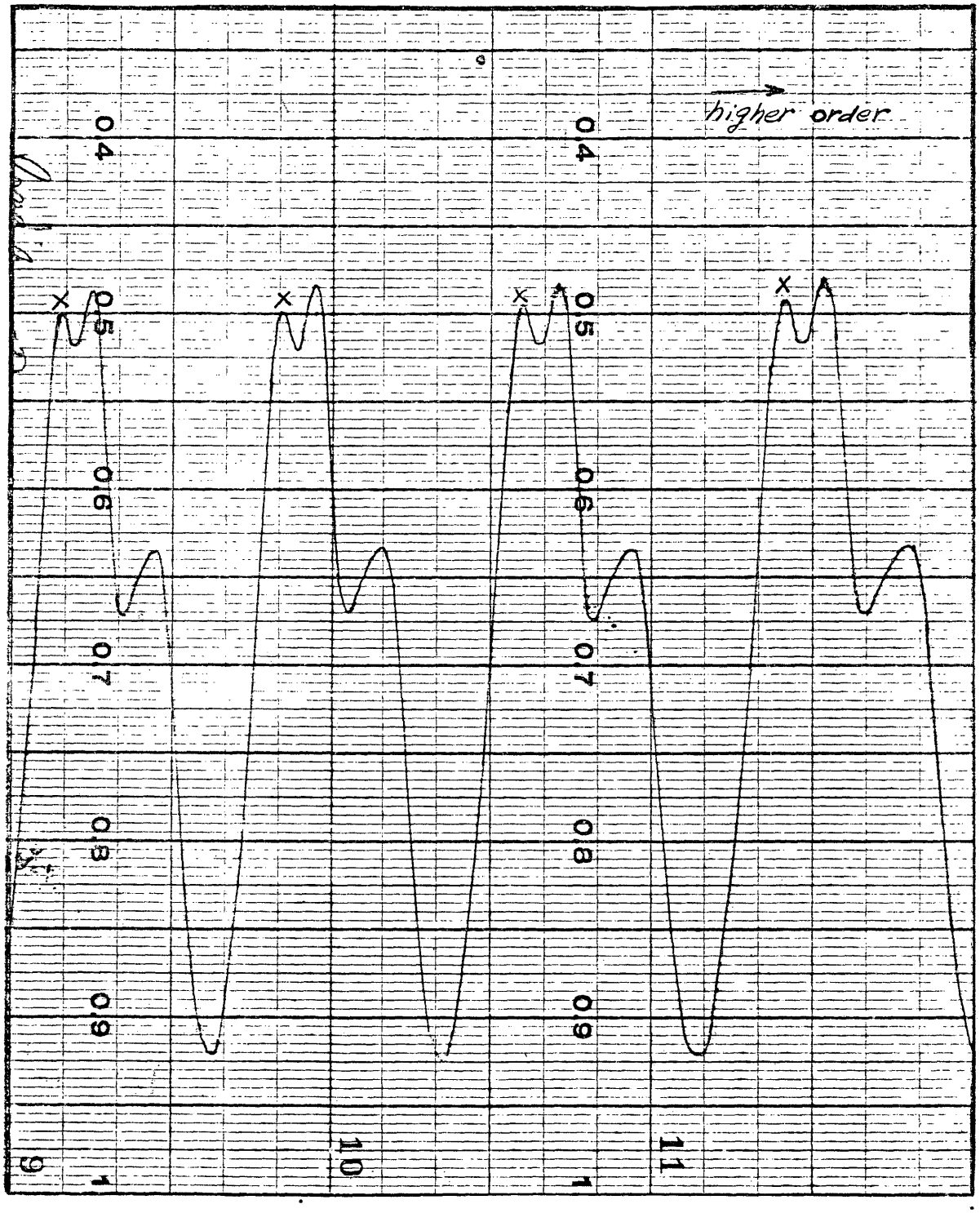

Fig.41 The Paschen-Back Pattern Scanning at 5.50 mm.

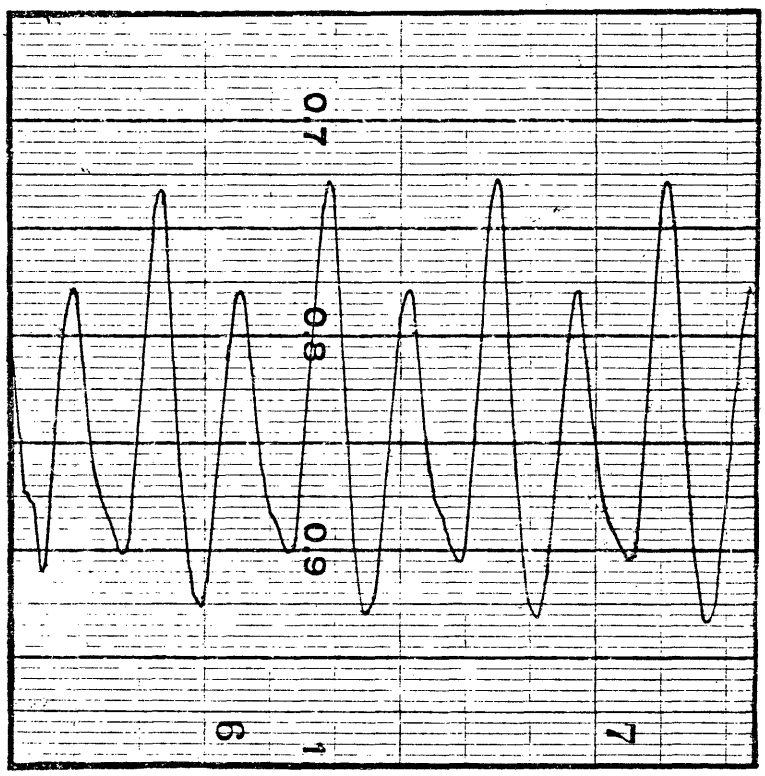

Fig.42 The s component of Fig.41.

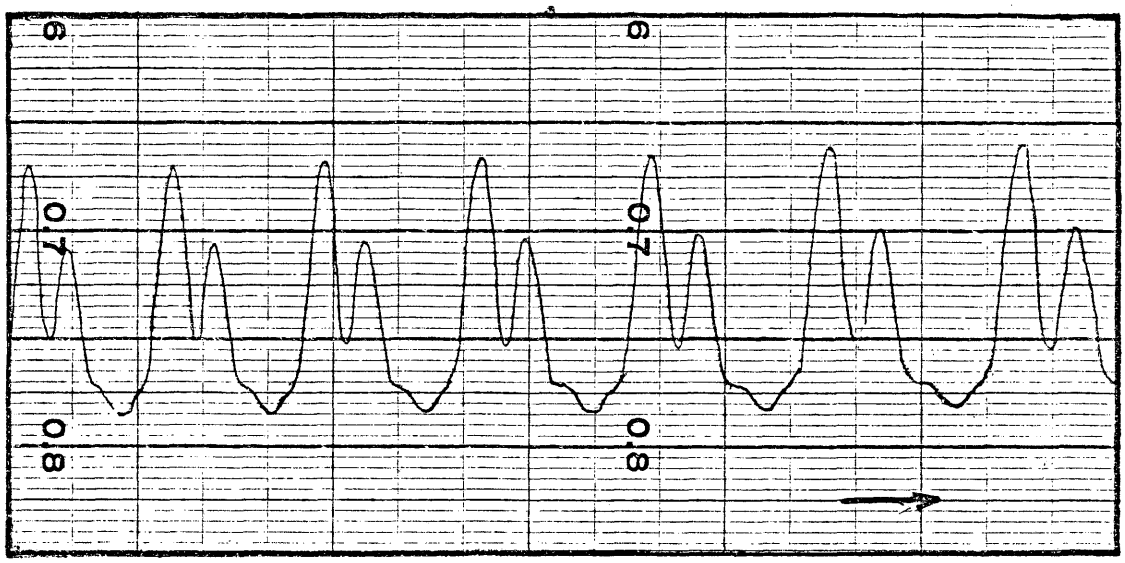

(a)

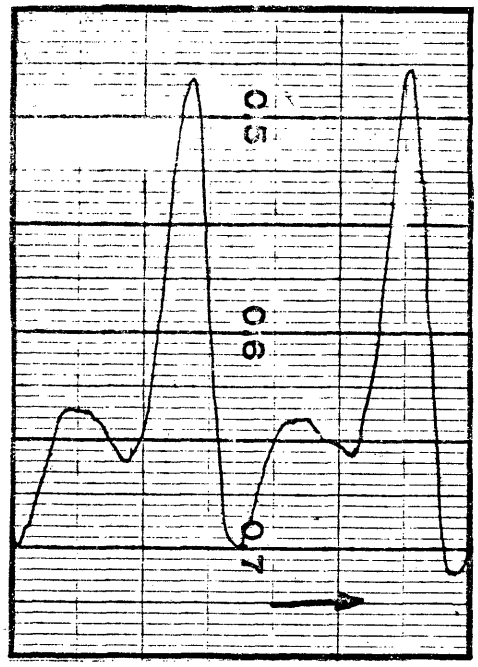

(b)

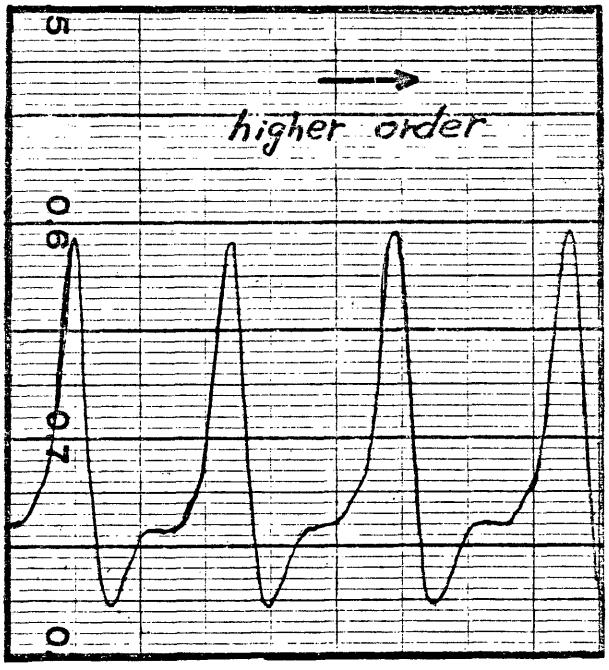

(c)

Fig.43 The scanning at interferometer spacing of (a) 8.24 mm,(b) 9.25 mm,(c) 9.50 mm.

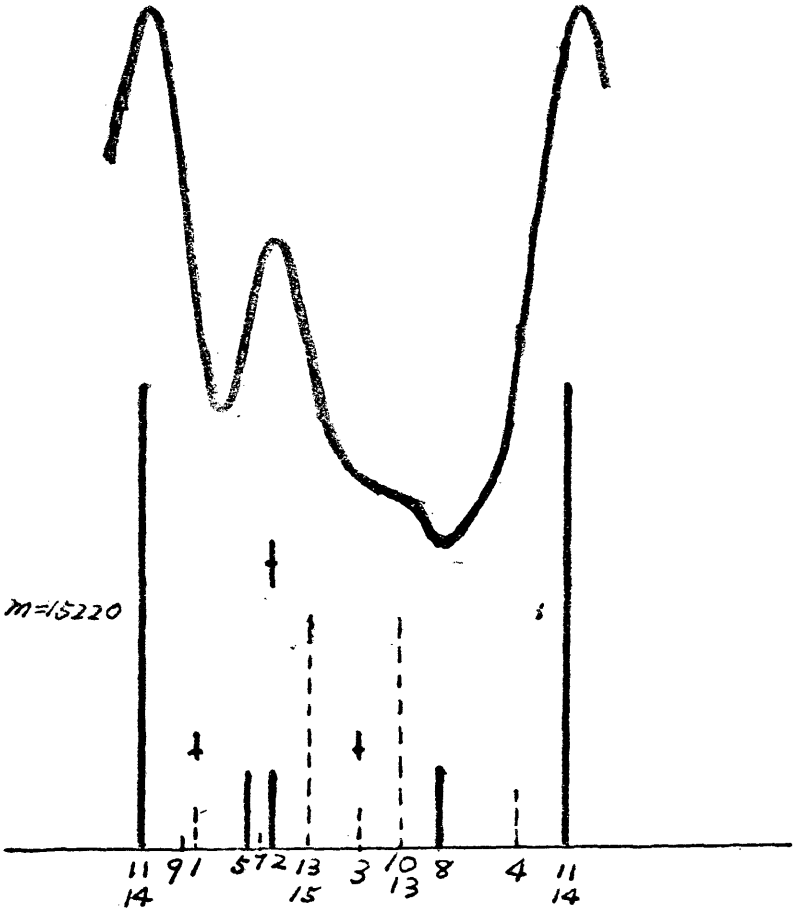

Fig.44 The Pattern at 8.24mm Spacing

V. DISCUSSION

The result of measuring Zeeman effect for He 2μ is quite satisfactory. This line is very sharp, Figure 32, and so the measurement is not difficult. In order to improve the agreement between measured and predicted splitting, a better measurement of the magnetic field is needed.

For the 1μ lines, the good resolution is impossible to obtain because components are too close to resolve and the self-reversal seriously upsets the intensity ratios. Use of a very thin light source could be helpful to reduce the self-reversal.

In the electronic detection system, the Syncroverter circuit and the Syncroverter could be replaced by a transistor switching circuit with same function. The open-closed resistance ratio is better for the Syncroverter, and at the moderate frequency used with PbS photocell,,and thus the Syncroverter has some advantage over a solid state device.

In its present form, the instrument works well and can now be applied to other spectral problems in the near infrared region. For absolute wavelength measurements it would be important to add a vacuum housing to remove the uncertainty due to air of variable composition and pressure.

REFERENCES

1. Mcgucken — Ninteenth-Century Spectroscopy, John-Hopkins Press (1969)
2. McQuister — Elements of IR Technology, John-Willy and Sons (1962)
3. Avery — Infrared Method, Academic Press (1960)
4. Hasmer — The Detection and Measurement of IR Radiation, Oxford (1957)
5. Delritz — Proc. IRE, 72, 1458 (1959)
6. Warrd — Proc. IRE, 72, 1470 (1959)
7. Hormig — Rev. Sci. Instru. 18, 7 (1947); 18,474 (1947)
8. Larmore — Proc. IRE, 72, 1987 (1959)
9. Morton — Proc. IRE, 72, 1467 (1959)
10. Hertz — Ann. d. Phys. 31, 983 (1887)
11. Einstein — Ann. d. Phys. 17, 132 (1905)
12. Millikan — Phys. Rev. 7, 362 (1916)
13. Moss — Proc. IRE, 43, 1869 (1955)
14. Levinstein — Proc. IRE, 72, 1478 (1959)
15. Cashman — Proc. IRE, 72, 1471 (1959)
16. Rieke — Proc. IRE, 72, 1475 (1959)
17. Slater — Phys. Rev. 103, 1631 (1956)
18. Harada — Phys. Rev. 102, 1258 (1956)
19. Hoods — Phys. Rev. 106, 502 (1957)
20. Petritz — Phys. Rev. 104, 1508 (1956); 105, 502 (1957)
21. Jones — Proc. IRE 72, 1481 (1959)
22. Spencer — Proc. IRE, 43, 2024 (1955)
23. Spencer — J. A. P. 31, 505 (1960)
24. Meissner — JOSA, 31, 405 (1941); 32, 185 (1942)
25. Candler — Modern Interferometer, Hilger and Watts (1951)
26. Steel — Interferometry, Cambridge (1967)

27. Humphreys Applied Optics, 2, 1155 (1963)
28. Jacquinot Rev. Progr. Phys. 23, 267 (1960)
29. Fabry Ann. Chim. et Phys. 25, 98 (1902); 16, 115 (1899)
30. Paschen Ann. d. Physik. 43, 858 (1914); 45, 625 (1914)
31. Ignatieff Ann. d. Physik 43, 1117 (1914)
32. Rao JOSA, 43, 952 (1953)
33. Jaffe JOSA, 43, 1170 (1953)
34. Jaffe Nature 168, 381 (1951); 175, 908 (1955)
35. Rank JOSA, 45, 636 (1955); 43, 952 (1953); 46, 477 (1956)
36. Ulrich IEEE Trans. 11, 363 (1963)
37. Moth Far IR Spectroscopy, Wiley-Interscience (1970)
38. Kruger Phys. Rev. 66, 855 (1930)
39. Ebbinghaus Ann. d. Phys. 7, 267 (1935)
40. Lamb Phys. Rev. 105, 559 (1957); 105, 573 (1957); 107, 125 (1957)
41. Uhlenbeck Nature 117, 264 (1926); Physika, 5, 266 (1925)
42. Gabuny Optical Physics, Academic Press (1967)
43. Ornstein Zeits. f. Phys. 22, 170 (1924); 24, 41 (1924)
44. White Introduction of Atomic Spectra, Mcgraw-Hill (1934)
45. Gottfried Quantum Mechanics (1965)
46. Condon Theory of Atomic Spectra, Cambridge (1933)
47. Bethe Handbuch der Physik, Band XXIV, Springer-Veglag (1933); Band XXXV, Springer-Veglag (1957)
48. Keesom Helium, Elesevier (1942)

49. Lohmann Phys. Zeits. 7, 809 (1906)
50. Briet Phys. Rev. 36, 383 (1929); 39, 616 (1932)
51. Steubing Ann. d. Phys. 24, 161 (1935); 30,1 (1937)
52. Stuart Roy. Soc. Proc. 131, 133 (1931)
53. Green Phys. Rev. 46, 888 (1934); 49, 632 (1936); 36, 157 (1936); 45, 632 (1934)
54. Heisenberg Zeits. f. Phys. 37, 263 (1926)
55. Darwin Roy. Soc. Proc. 115, 1 (1927); 118, 264 (1927)
56. Houston Phys. Rev. 33, 297 (1927)
57. Kline Doctoral Thesis, Purdue University (1952)
58. Diefenderfer Principle of Electronic Intrumentation, Saunders (1972)
59. Gibson Control System Components, McGraw-Hill (1958)
60. Barna Operational Amplifier, Wiley-Interscience (1971)
61. Smith Modern Operational Circuit Design (1971)
62. PAR Instruction Manual, Lock-in Amplifier Model JB-4, Princeton Applied Research.
63. Houston Phys. Rev. 29, 478 (1926)
64. Ditchburn Light, Wiley (1968)
65. Megger Jour. R. Bur. Std. 14, 487 (1935); 39, 121 (1932)
66. Zaidel Tables of Spectral Lines, IFI/PLENUM (1970)